PHYSICAL REVIEW X **14,** 041002 (2024)

Active Fréedericksz Transition in Active Nematic Droplets

Salman Alam,[1] Bibi Najma,[1] Abhinav Singh,[2,3,4] Jeremy Laprade,[1] Gauri Gajeshwar,[1]
Hannah G. Yevick,[1] Aparna Baskaran,[1] Peter J. Foster,[1,†] and Guillaume Duclos[1,*]

[1]*Department of Physics, Brandeis University, Waltham, Massachusetts 02453, USA*
[2]*Faculty of Computer Science, Technische Universität Dresden, Dresden, Germany*
[3]*Max Planck Institute of Molecular Cell Biology and Genetics, Dresden, Germany*
[4]*Center for Systems Biology Dresden, Dresden, Germany*

(Received 26 October 2023; revised 3 May 2024; accepted 31 July 2024; published 3 October 2024)

Active nematic liquid crystals have the remarkable ability to spontaneously deform and flow in the absence of any external driving force. While living materials with orientational order, such as the mitotic spindle, can self-assemble in quiescent active phases, reconstituted active systems often display chaotic, periodic, or circulating flows under confinement. Quiescent *in vitro* active nematics are, therefore, quite rare, despite the prediction from active hydrodynamic theory that confinement between two parallel plates can suppress flows. This spontaneous flow transition—named the active Fréedericksz transition by analogy with the conventional Fréedericksz transition in passive nematic liquid crystals under a magnetic field—has been a cornerstone of the field of active matter. Here, we report experimental evidence that confinement in spherical droplets can stabilize the otherwise chaotic dynamics of a 3D extensile active nematics, giving rise to a quiescent—yet still out-of-equilibrium—nematic liquid crystal. The active nematics spontaneously flow when confined in larger droplets. The composite nature of our model system composed of extensile bundles of microtubules and molecular motors dispersed in a passive colloidal liquid crystal allows us to demonstrate how the interplay of activity, nematic elasticity, and confinement impacts the spontaneous flow transition. The critical diameter increases when motor concentration decreases or nematic elasticity increases. Experiments and simulations also demonstrate that the critical confinement depends on the confining geometry, with the critical diameter in droplets being larger than the critical width in channels. Biochemical assays reveal that neither confinement nor nematic elasticity impacts the energy-consumption rate, confirming that the quiescent active phase is the stable out-of-equilibrium phase predicted theoretically. Further experiments in dense arrays of monodisperse droplets show that fluctuations in the droplet composition can smooth the flow transition close to the critical diameter. In conclusion, our work provides experimental validation of the active Fréedericksz transition in 3D active nematics, with potential applications in human health, ecology, and soft robotics.

DOI: 10.1103/PhysRevX.14.041002 Subject Areas: Biological Physics, Soft Matter

I. INTRODUCTION

Active nematics are dense suspensions of motile and locally aligned rodlike units [1–3]. This class of material includes diverse synthetic and biological systems, including vibrated granular rods [4], multicellular tissues [5–7], bacterial biofilms [8–11], and the mitotic spindle [12], a dense suspension of biopolymers called microtubules driven out of equilibrium by motor proteins. Unconfined, active nematics are intrinsically unstable [13]: Active stresses generated by the constitutive energy-consuming mesogens drive the spontaneous growth of long-wavelength deformations and the nucleation of topological defects at any nonzero activity. When confined between two parallel plates, active nematics cannot deform freely anymore because boundaries impose constraints on hydrodynamic flows [14–17]. Consequently, active stresses must overcome both nematic elastic relaxation and viscous dissipation to spontaneously deform the confined nematic phase. Above that critical activity, self-amplifying deformations with a finite wavelength destroy the long-range nematic order [16,17], leading to various flowing states, including chaotic flows at high activity [18].

The activity-dependent bifurcation between a quiescent homogeneously aligned active phase and a spontaneously

---

[*] Contact author: gduclos@brandeis.edu

[†] Present address: Department of Physics and Astronomy, Bridge Institute, Michelson Center for Convergent Bioscience, University of Southern California, Los Angeles, California 90089, USA.

flowing and nonhomogeneously aligned active phase is called the active Fréedericksz transition [14,15,19] by analogy with the conventional Fréedericksz transition in passive liquid crystals [20,21]. First observed in 1927, the passive Fréedericksz transition is triggered when a sufficiently strong electric or magnetic field is applied in a direction orthogonal to the nematic director of a liquid crystal confined between two parallel plates. At low values of applied field strength, the nematic remains orthogonal to the external field. Above a critical field strength, the nematic director aligns with the field. The critical field magnitude depends on the nematic elasticity of the liquid crystal and on confinement. Both the active and the passive Fréedericksz transitions describe a bifurcation from a homogeneous to a nonhomogeneous alignment. Two main differences are that (i) the active transition is driven by internally generated active stress rather than by an external field, and (ii) the resultant distorted active phase spontaneously flows. The impact of the passive Fréedericksz transition was transformative for the field of liquid crystals. It enabled electro-optic switching control, leading to modern LCD technology. Similarly, harnessing the active Fréedericksz transition in confined active nematics will open the road to diverse engineering applications for low-Reynolds active fluids that require controlling active flows. A better understanding of the physical mechanisms at play in the collective movements of active mesogens could also have biomedical and ecological applications, including preventing the migration of sarcoma cells from primary tumors [15] or the spreading and growth of bacterial biofilms [8–11], two well-characterized examples of active nematics.

Confinement is known to transform the inherently chaotic dynamics of active fluids with orientational order. For example, confinement in three-dimensional annular channels can convert chaotic flows into long-ranged coherent flows [22–27]. In two-dimensional active nematics, confinement in disks and tracks also demonstrates how to tame chaotic flows to produce either circulating [28], periodically self-shearing [29], or other periodic flow patterns [30–33]. However, these experimental achievements do not directly test the theoretical predictions of the active Fréedericksz transition between a spontaneously flowing and a quiescent state. They instead validate another theoretically predicted transition between two flowing states, from chaotic to laminar flow. To date, to our knowledge, there has been no experimental evidence that confinement can stabilize an extensile active nematic phase, suppressing all unstable modes to give rise to a quiescent—yet still out-of-equilibrium—nematic liquid crystal. Furthermore, the impact of curved confining geometries on the Fréedericksz transition has been underexplored despite the fact that most experimental realizations of confined active fluids have curved boundaries that preclude homogeneous alignment. As a result, it is unclear whether spherical confinement, where the ground state is not homogeneously aligned, modifies the theoretical predictions that result from linearizing the active nematohydrodynamic equations around a homogeneously aligned state [14,15,19].

We previously reported an analogous flow transition in two-dimensional contractile active nematics composed of motile cells confined in tracks of increasing width [15]. Above a critical width, the nematic tissue undergoes a transition from a nonflowing homogeneously aligned nematic to a spontaneously flowing nonhomogeneously aligned tissue. However, the lack of control over cells' activity, effective nematic elasticity, and their coupling through cell density limited the exploration of the nonequilibrium phase diagram. Tunable active liquid crystals with independent control over activity and nematic elasticity are required to measure the system's dynamics close to the bifurcation point and test the predictions of the active hydrodynamic theory.

In vitro reconstituted active liquid crystals offer an experimental path forward [34,35]. In the past decade, dense extensile bundles of molecular motor clusters and microtubules depleted on an oil-water interface have been adopted as a model system for studying the emergent properties of 2D active nematics [28,29,33,34,36–40]. However, limitations resulting from the composition of 2D microtubule-based active nematics preclude quantitatively testing the active Fréedericksz transition:

(i) First, all the mesogens are active. As a result, active and elastic stresses are coupled, limiting the phase-space exploration.
(ii) Second, the nematic elastic constants of a microtubule-based active nematic are unknown, in part because microtubules form bundles whose structure and mechanical properties are still under study [41].
(iii) Third, viscous damping by the oil-layer screens hydrodynamic flows in the 2D active layer, fundamentally changing the transition's nature and the emergent dynamics at the bifurcation point [40].

Here, we overcome these challenges by assembling a 3D active composite nematic liquid crystal by dispersing dilute active biopolymers (approximately 0.1% volume fraction) [18] in a dense 3D passive colloidal liquid crystal (approximately 2.2% to 5.5% volume fraction) [42] [Fig. 1(a)]. We use semiflexible fd viruses as a well-characterized and tunable model system for a liquid-crystalline background [43]. Nematic elasticity increases nonlinearly with fd virus concentration [43]. The active biopolymers are kinesin microtubules bundled by PRC1 [Fig. 1(b)], a diffusible cross-linking protein that still allows relative sliding of the filaments [44,45]. Without PRC1, the microtubules would be homogeneously distributed and coaligned with the passive nematic background, but would not form stress-generating bundles. This microtubule-specific cross-linker can replace the conventional nonspecific bundling depletant previously used in microtubule-based active

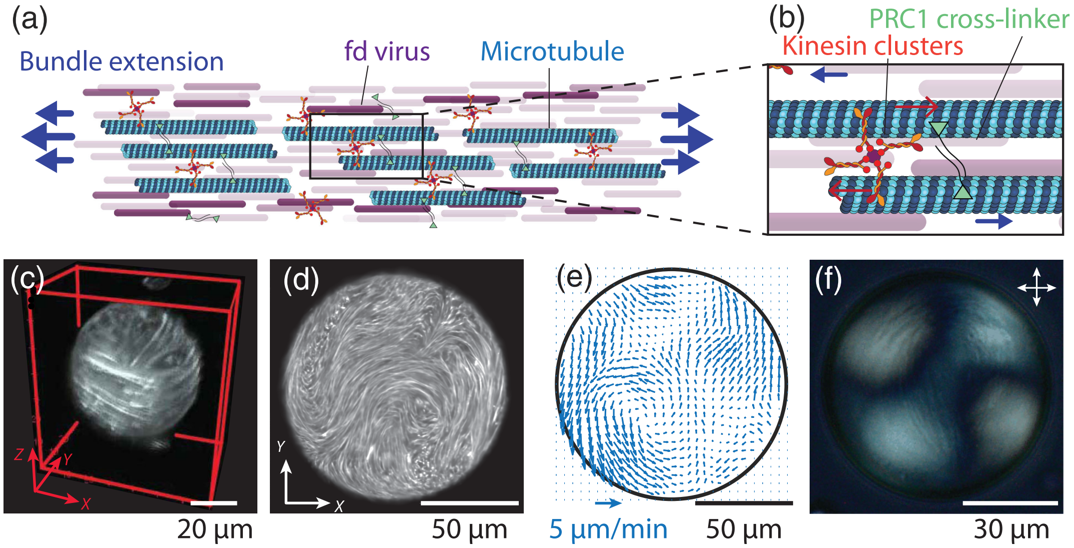

FIG. 1. Spontaneous flows in 3D active nematics confined in droplets. (a) Schematic of an extensile kinesin-microtubule bundle dispersed in a nematic liquid crystal composed of elongated fd viruses. (b) Close-up of the multivalent clusters of kinesin-1 motors and the microtubule cross-linkers. Kinesin-1 motor clusters walk toward the plus end of the microtubules. PRC1 is a diffusive cross-linker that bundles microtubules. (c) 3D reconstruction of the microtubule bundles at the surface of the droplet. (d) Confocal imaging of the midplane of a 3D active nematic droplet. Microtubules are fluorescently labeled. (e) Instantaneous flow field corresponding to panel (d) measured with particle image velocimetry. (f) 3D active nematic droplet imaged with polarized microscopy. Birefringence indicates local nematic order.

fluids [46]. This recent development enabled the dispersion of active microtubule bundles into nematic liquid crystals [42] and passive gels of actin filaments [47] while avoiding the aggregation of the passive colloidal rods that would have occurred due to nonspecific depletion. The microtubule bundles generate extensile active stresses, continuously elongating as clusters of kinesin motors hydrolyze adenosine 5’-triphosphate (ATP) to step along and slide apart adjacent antiparallel microtubules [Fig. 1(b)]. Recent experiments demonstrate that active stress increases when the concentration of motor clusters increases [48,49]. The active microtubule bundles and the passive colloidal rods are fully miscible, coaligned, and no demixing is observed while the system is active [42]. The bundles’ elongation drives the emergence of collective flows that advect the passive colloidal rods and deform the nematic liquid crystal. Despite the composite nature of this material, it is unclear if active and passive stresses are fully decoupled because of the biochemical nature of how active stress is generated. First, while motor clusters generate active stresses, they can also contribute to nematic elasticity by cross-linking microtubules [49–51]. Second, the passive liquid crystals might impact how motor clusters step onto microtubules at the microscopic level. Kinesin-1 molecular motors are known to walk at different speeds under load [52], and the presence of passive nematogens might impact the motors’ ability to generate active stresses.

Here, we confine such 3D active nematics in spherical droplets to investigate how the interplay of activity, nematic elasticity, and confinement impacts the spontaneous flows that are ubiquitous in active nematics. Experiments demonstrate the existence of a critical diameter below which spontaneous flows are suppressed (Sec. II A). We find that (i) the critical confinement decreases when motor cluster concentration is increased, when nematic elasticity is decreased, or when the confining geometry is changed from droplets to channels (Sec. II B). (ii) Quantitative measurements of the ATP-hydrolysis rate demonstrate that neither the presence of passive colloidal rods nor confinement impacts how molecular motors walk on microtubules. High-magnification microscopy shows that the microtubules are still sliding along the bundles in the quiescent active phase. Consequently, we can conclude that the quiescent droplets are in the stable out-of-equilibrium phase predicted by the active hydrodynamic theory (Sec. II C). (iii) Fluctuations in flow speed result from fluctuations in the composition of the composite 3D active nematics, which smooth the transition and explain the apparent multistability close to the bifurcation point (Sec. II D). Taken together, these findings provide experimental validation for the active Fréedericksz transition in 3D extensile active nematics, advancing our understanding of the onset of low-Reynolds-number turbulence in 3D active nematics.

II. RESULTS

A. Spontaneous flow transition as the droplet’s diameter is increased

We confined the biomimetic 3D active nematic phase in a water-in-oil emulsion (Appendix A). 3D reconstruction of the microtubules from confocal imaging showed that the surface anchoring at the oil-water interface was planar [Fig. 1(c)]. We first imaged large-diameter active droplets (approximately 100 μm in diameter [Fig. 1(d), Video S1 [53]]. Flows were measured using particle image velocimetry [PIV, Fig. 1(e), Appendix A], and the mean flow speed was found to be independent of whether the active nematic was confined in droplets or channels of similar sizes (Fig. 11). Birefringence of the composite material when imaged using polarized light microscopy indicates local nematic order [Fig. 1(f)], in contrast to microtubule-based active fluids lacking the passive colloidal liquid-crystalline background [18].

We then produced polydisperse emulsions to test how spherical confinement impacts the emergence of active flows [Fig. 2(a), Video S2 [53]]. The droplets' diameters ranged from 30 to 550 μm. We replaced the ATP with a caged ATP, whose caging group can be photolyzed upon exposure to UV light. This enabled the synchronization of ATP hydrolysis in all the active droplets once the emulsion was formed and the sample was under the microscope. We segmented the droplets and measured the flow statistics using PIV (Fig. 13, Appendix A). Figure 2(b) shows the time-averaged speed in the segmented droplets. Large droplets started to spontaneously flow after uncaging ATP, reaching their steady-state flow speed after ten

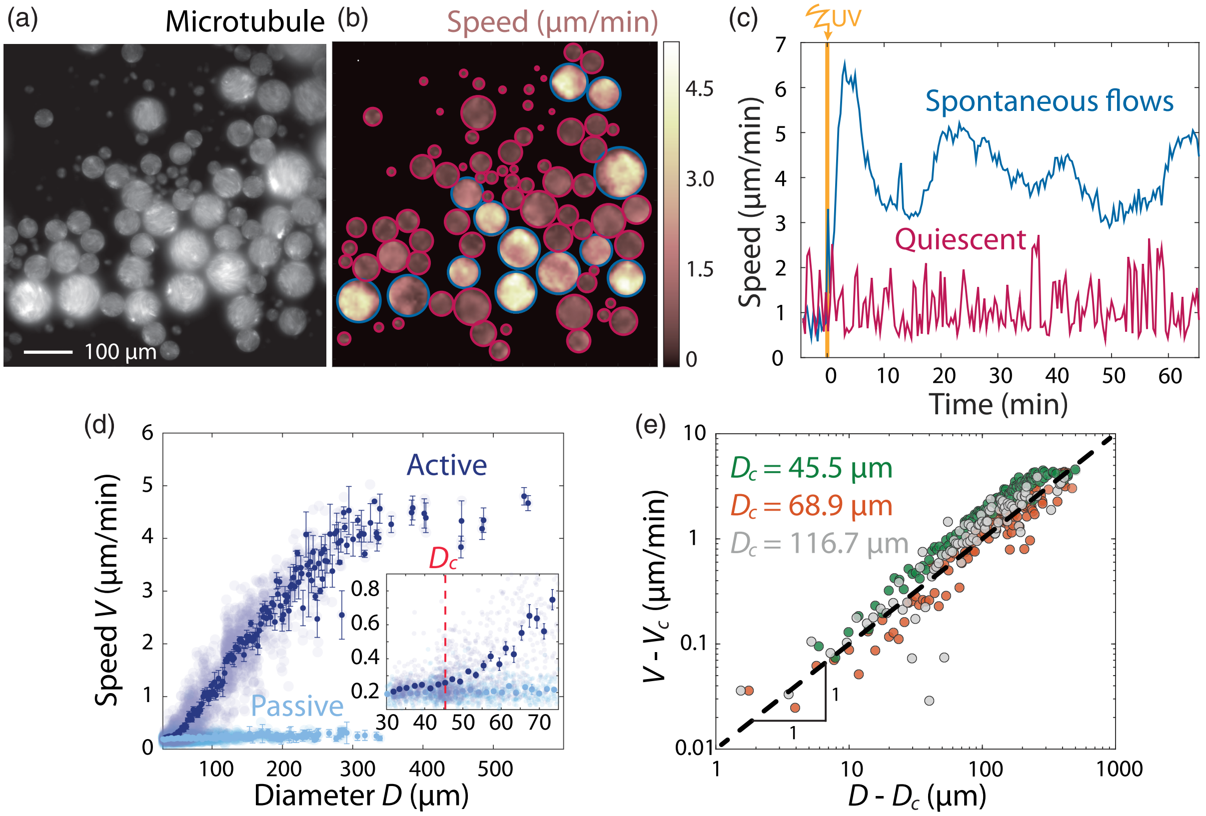

FIG. 2. Spherical confinement controls a transition from a quiescent to a spontaneously flowing phase. (a) Polydisperse 3D active nematic droplets imaged with widefield fluorescence microscopy. (b) Time-averaged speed of the active flows in the polydisperse emulsion shown in panel (a). Droplets circled in red are quiescent, while droplets circled in blue are spontaneously flowing. (c) Speed versus time plot for two individual droplets of different diameters. The red curve corresponds to a quiescent active droplet of diameter $D = 41$ μm, and the blue curve corresponds to a spontaneously flowing droplet of diameter $D = 89$ μm. Both droplets are in the same field of view shown in panels (a) and (b). ATP is uncaged at $t = 0$ min. (d) Lin-lin plot of the time-averaged speed of the 3D active nematics droplets as a function of their diameter. Active droplets are in dark blue, and passive droplets that lack molecular motors are in light blue. Each semitransparent disk represents the speed of a single droplet averaged over 60 minutes ($N = 2582$ active droplets, $N = 1400$ passive droplets). Each dark disk and the error bars represent the mean, and the standard deviation of the droplets' speed binned over a 2-μm-diameter interval. The flow speed saturates for droplets with a diameter above 400 μm. Inset: Enlargement of the speed versus diameter plot highlighting where the transition from quiescence to spontaneous flow occurs. The red dashed line shows the critical diameter $D_c = 45.5$ μm over which the flows in the active and passive droplets are statistically different from one another (student *t*-test on the binned speed distributions). (e) Log-log plot of the flow speed versus droplet diameter in the spontaneous flow regime for three independent samples with different critical diameters D_c. The dashed line has a slope of 1. Motor clusters = 25 nM for the orange and gray curves, 35 nM for the green curve, fd virus = 40 mg/mL.

minutes [Fig. 2(c)]. Small droplets are quiescent: Uncaging ATP did not produce any persistent flows despite the presence of motor clusters and microtubule bundles. The nonzero flow speed measured in the small quiescent droplets came from fluctuations of the microtubule bundles and from noise from the PIV measurement. Importantly, the morphological features of the kinesin-microtubule bundles did not change above and below D_c (Fig. 9). We measured the flow speed in over 2500 active droplets and found the existence of a critical diameter below which active droplets of 3D active nematics were not flowing [Fig. 2(d)]. A statistical test that detected when the flows in active droplets started to differ from the flows in passive droplets with no molecular motors provided a robust metric to measure the critical diameter [Fig. 2(d), inset, Fig. 14, Appendix A]. Above the critical diameter, the average flow speed scaled linearly with droplet size, irrespective of the composition of the active phase and the value of the critical diameter [Fig. 2(e)].

B. Critical diameter depends on the composition of the 3D active nematic and on the confining geometry

Next, we systematically changed the composition of the 3D active nematic to study how the interplay of activity, nematic elasticity, and confinement controlled the spontaneous flow transition. We found that the critical diameter decreased as the concentration of motor clusters was increased [Fig. 3(a)]. This result was consistent with recent experiments in 3D microtubule-based active fluids that demonstrated that the magnitude of the active stress increased when motor concentration was increased [48,49] and with theoretical predictions that the active length scale decreased when activity was increased [54]. We additionally found that the critical diameter increased as the concentration of fd viruses was increased [Fig. 3(b)]. This result was consistent with experiments with passive fd-based liquid crystals where nematic elasticity increased with increasing fd concentration [43] and with theoretical predictions for 2D active nematics where the active length scale increased when nematic elasticity was increased [54]. We further showed that these experimental results were also consistent with numerical simulations of an active 3D Erickson-Leslie hydrodynamic model of active nematics confined in spherical droplets [19] (Fig. 4, Appendix B): Increasing the droplet diameter led to a transition from a quiescent phase to a spontaneously flowing phase [Figs. 4(a)–4(d), Video S3 [53]], and the critical diameter increased when the ratio of nematic elasticity over activity increased [Fig. 4(e)]. Furthermore, increasing the activity midway throughout the simulations demonstrated that individual droplets underwent the active Fréedericksz transition from a quiescent phase to a flowing phase as soon as activity was increased above the critical activity (Video S4 [53]).

We further studied this model to understand better the effect of the confining geometry on the active Fréedericksz transition. Comparing the results of the numerical simulations in droplets to an analytical calculation in channels [19] suggested that the critical width for active nematics confined in channels was smaller than when confined in droplets [Fig. 4(e)]. We confirmed this prediction experimentally: For the same confining length, active droplets were quiescent, while homogeneously aligned active slabs were unstable and underwent the well-characterized bend instability [16] (Fig. 12, Video S5 [53]).

We then quantified the dynamics of the active droplets in the spontaneously flowing phase. We performed experiments with monodisperse active droplets created with a microfluidic droplet generator [Fig. 5(a)] [55]. The active nematic droplets were slightly larger than the critical diameter and temporally averaged the flow fields ($D/D_c \sim 1.3$). We measured the azimuthal component of

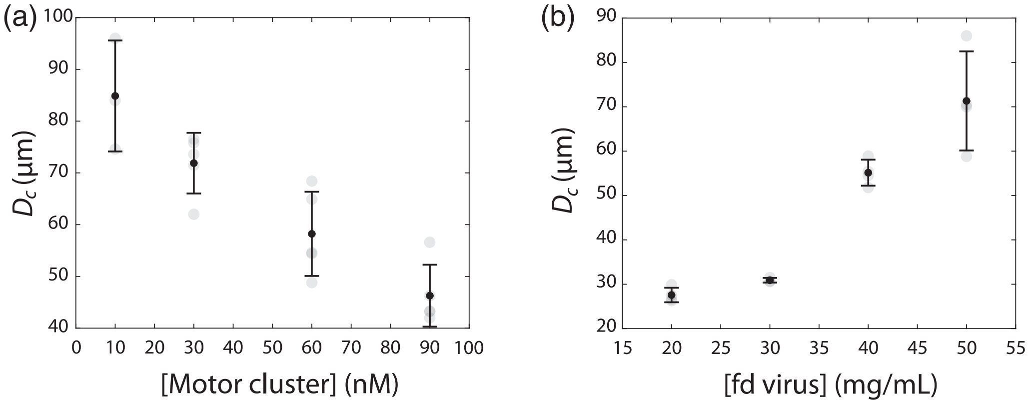

FIG. 3. The critical diameter depends on the composition of the 3D active nematic. (a) Critical diameter decreases when the concentration of motor clusters is increased. (b) The critical diameter increases when the concentration of fd viruses is increased. Each semitransparent disk represents an independent experiment ($N = 3$ to 5 replicates for each experimental condition). The black disks and the error bars correspond to the mean and the standard deviation over the independent replicates. [MT] = 1.3 mg/mL, [ATP] = 1.4 mM. [In] (a), [fd virus] = 40 mg/mL. In (b), [motor clusters] = 30 nM.

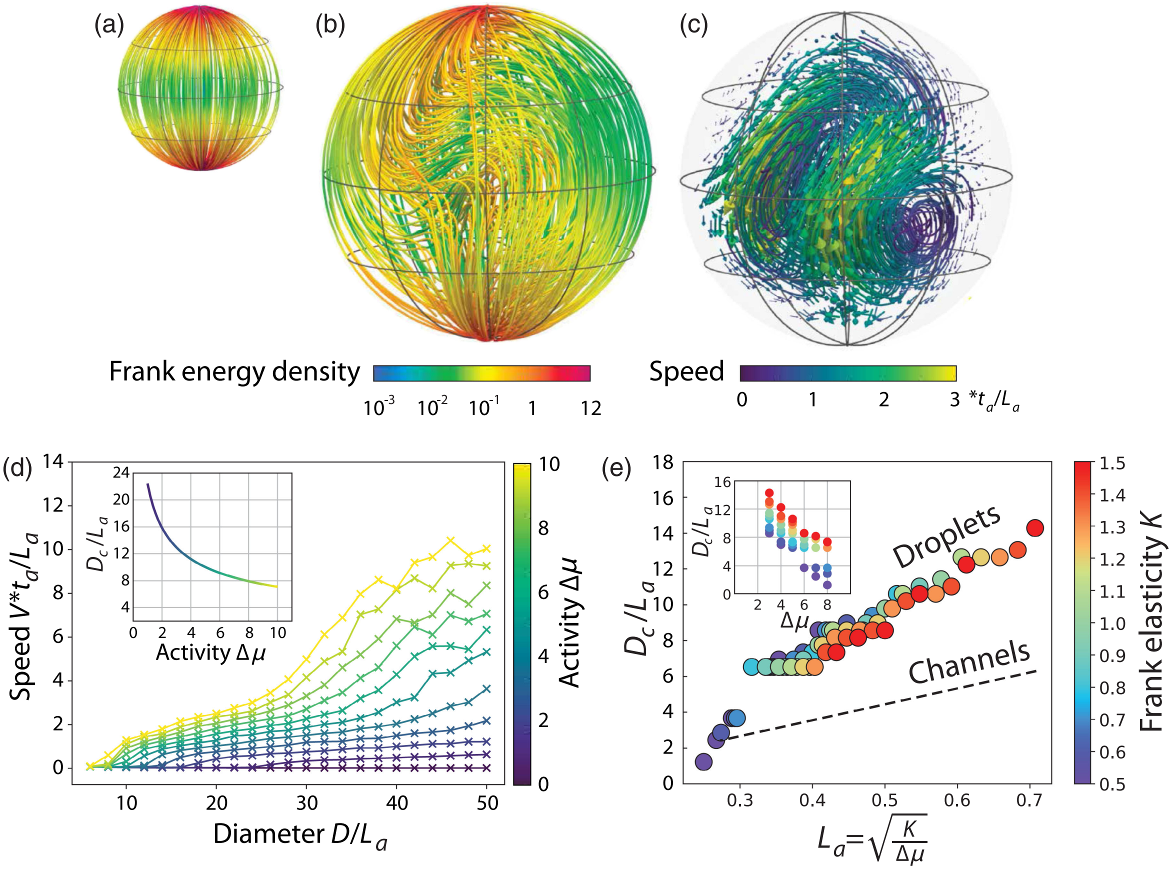

FIG. 4. Simulations of 3D active nematics confined in droplets. Orientation field and Frank energy density in (a) a quiescent active droplet ($D = 4 < D_c$) and (b) a spontaneously flowing drop ($D = 8 > D_c$). (c) Flow field in the flowing active droplet. (d) Speed versus diameter plot. The color bar shows various activity levels. Inset shows how the critical diameter D_c varies with activity. (e) Plot of the critical diameter as a function of the active length L_a. The color bar shows various nematic elasticities. Inset: critical diameter as a function of the activity. The critical diameter is systematically larger than the critical width for 3D active nematics with the same activity and nematic elasticity confined in channels. The dashed line shows the results from linear stability analysis performed in Ref. [19]. All times and distances are shown in units of the active timescale $t_a = (1/\Delta\mu)$ and the active length scale $L_a = \sqrt{K/\Delta\mu}$. Parameters used unless indicated otherwise in the figure are $L_a = \sqrt{0.3} = 0.548$, $K = 1.5$, $\Delta\mu = 5$, $\zeta = 1$, $\gamma = 1$, $\eta = 1$, $\lambda = 0$, and $\nu = -1$.

the in-plane flows and found that the flows were slower at the center and edges of the droplet and faster on a corona with an inner radius of $R/2$ [Figs. 5(a)–5(c)]. This is consistent with circulating flows seen previously for 3D active isotropic fluids confined in cylinders [22], dense circulating suspensions of bacteria confined in droplets [23], and for 2D active nematics confined in disks [28]. For active droplets much larger than D_c ($D/D_c \geq 2$), the flows were not structured anymore [Fig. 5(d)]. The hydrodynamic model showed a similar transition with circulating flows when the diameter was close to D_c ($D/D_c \sim 1.3$), and unstructured chaotic flows when the diameter was much larger than D_c [$D/D_c \geq 2.5$, Figs. 5(e)–5(g), Fig. 15]. This transition is reminiscent of the transition from self-sharing to chaotic flows, which was previously reported in simulations of 3D active nematics confined between two parallel plates [19,93] and in confined 2D active nematics [29].

While this model extends the predictions of the active Fréedericksz transition to 3D active nematics confined in droplets, specificities of how molecular motors generate active stresses require some further biochemical investigation before concluding that this spontaneous flow transition is an experimental realization of the seminal active Fréedericksz transition. Indeed, the presence of passive nematogens and confinement might impact how molecular motors and microtubule bundles generate stresses, given that molecular motors are known to adjust their stepping rate and even stall depending on the load they push against [52]. We can, therefore, identify two hypotheses: (i) The highly confined active phase is quiescent because the motors are stalled, they do not step on microtubules, which form a passive nematic phase, or (ii) the active phase is quiescent because the active stress cannot overcome the passive nematic stress that increases when confinement and nematic elasticity increase. In that case, the quiescent phase

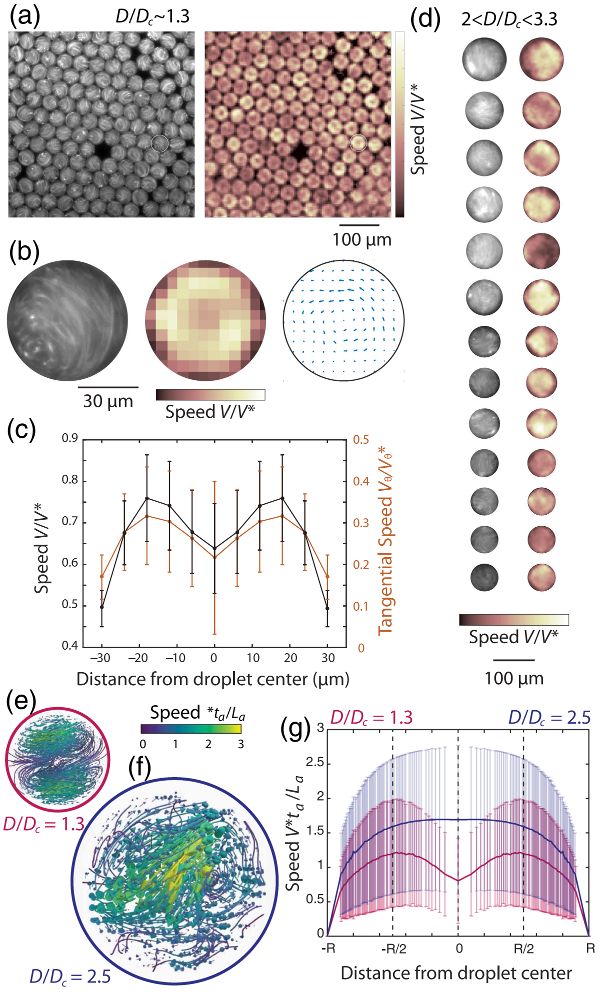

FIG. 5. Quantitative analysis of the dynamics of spontaneously flowing droplets in experiments and simulations. (a) Array of monodisperse spontaneously flowing active droplets; diameter $D = 60.4 \pm 0.5$ µm (mean ± s.d.); $D_c = 45.5$ µm; $D/D_c \sim 1.3$. The right panel shows a fluorescent image of the microtubules, and the left panel shows the time-averaged flow speed for the same field of view. (b) Enlargement of an individual droplet, the time-averaged flow speed, and the time-averaged velocity field. (c) Radial dependence of the speed and the azimuthal speed for spontaneously flowing active droplets with $D/D_c \sim 1.3$. (d) Fluorescence image and time-averaged flow speed or spontaneously flowing active droplets with $2 \leq D/D_c \leq 3.3$. The same data are shown in Figs. 2(a) and 2(b). Instantaneous velocity field in simulated active nematic droplets with diameter (e) $D/D_c = 1.3$ and (f) $D/D_c = 2.5$. (g) Time-averaged and spatially averaged rms speed in simulated spontaneously flowing active droplets. Error bars show standard deviation from time averaging.

is still out of equilibrium, and activity does not depend on confinement or nematic elasticity. To distinguish between those two scenarios, we performed biochemical assays to measure how the rate of ATP hydrolysis, which characterizes how motors walk on microtubules, depends on confinement and nematic elasticity.

C. ATP-hydrolysis rate is independent of nematic elasticity and confinement

We tested whether the quiescent phase could result from a decrease in the stepping rate of motors onto microtubules because of confinement and/or the presence of passive nematogens. To test this hypothesis, we measured how the ATP consumption rate depended on the concentration of fd viruses and on confinement using biochemical assays. We measured the fluorescence intensity of nicotinamide adenine dinucleotide (NADH) [56–58], a fluorophore-coupled reporter system for ATP hydrolysis [Fig. 6(a)]. Pyruvate is a by-product of the ATP regeneration reaction, which maintains a constant ATP concentration throughout the experiment. Pyruvate is coupled to a redox reaction that converts NADH into NAD^+. NADH is an endogenous fluorophore with an excitation band centered in the UV (340 nm), while NAD^+ fluoresces only in the deep UV (260 nm). When one molecule of ATP is hydrolyzed by a kinesin stepping on a microtubule, one molecule of NADH is oxidized, and the fluorescent intensity of the active sample in the UV decreases accordingly. Quantification of NADH consumption using spectroscopy is a standard and sensitive biochemistry technique to measure ATPase activity. We concomitantly measured the NADH fluorescent intensity and imaged the microtubule bundles in 3D active nematic droplets. We first focused on large spontaneously flowing droplets ($D > D_c$). Upon uncaging ATP, active droplets showed a linear decrease of NADH fluorescence over time [Fig. 6(b)], while the fluorescent intensity of passive droplets that were lacking molecular motors was constant over time [Fig. 6(c)]. The ATP-hydrolysis rate was proportional to the slope of the linear decay of the NADH intensity over time. Here, 2.5 mM of NADH was consumed in 4.5 h, which was shorter than the lifetime of the sample [Fig. 6(e)]. The ATP-hydrolysis rate was constant over that duration. PIV analysis of the microtubule channel confirmed that active nematics confined in droplets were spontaneously flowing while the passive droplets were static [Fig. 6(d)]. The NADH-coupled ATPase fluorescent assay gave similar ATP-hydrolysis rates as the well-established phosphate assay, an end-point assay that measures the production of inorganic phosphate generated during ATP hydrolysis (Fig. 10, Appendix A).

Measuring the rate of ATP hydrolysis while titrating the concentration of fd viruses demonstrated that the presence of passive mesogens did not impact how chemical energy was consumed. The ATP-hydrolysis rate was identical for active isotropic fluids assembled in the absence of fd viruses and for active nematics composed of up to 45 mg/ml of fd viruses [Fig. 6(f)]. Second, the ATP-hydrolysis rate was independent of the droplet's diameter, or the confining geometry (channel vs droplet). We binned the data into three groups: quiescent active droplets, spontaneously flowing active droplets, and spontaneously flowing active phase in a channel. Statistical analysis

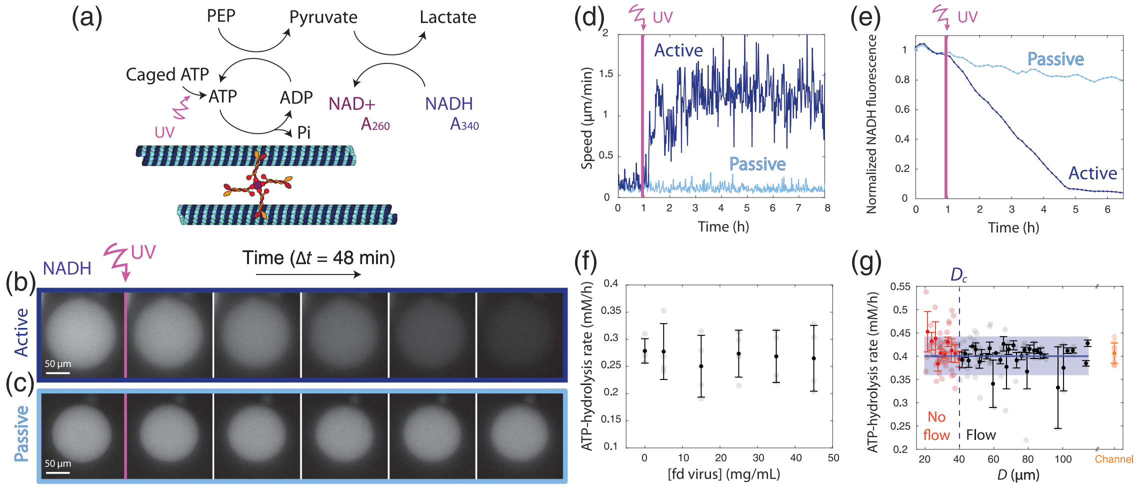

FIG. 6. The ATP-hydrolysis rate of the 3D active nematics does not depend on confinement or on the concentration of viruses in the nematic background. (a) Biochemistry of the reporter system where ATP regeneration is coupled to NADH fluorescence. (b),(c) Time series of the NADH fluorescent signal for (b) active and (c) passive droplets with no molecular motor clusters. Droplets are activated when ATP is uncaged. (d) Speed vs time plot for the active and passive droplets shown in (b) and (c) (speed of individual droplets only). (e) Normalized NADH signal over six hours for the active and passive droplets shown in (b) and (c). The slope of the linear decay after uncaging ATP is proportional to the ATP-hydrolysis rate. (f) ATP-hydrolysis rate when the concentration of fd viruses is increased. The sample is in the isotropic phase below 22 mg/ml and in the nematic phase above. Each semitransparent disk represents an independent experiment ($N = 4$ replicates). The black disks and the error bars correspond to the mean and the standard deviation over the independent replicates. (g) ATP-hydrolysis rate as a function of the confinement for 3D active nematic droplets. Both quiescent ($D < D_c$, red disks) and spontaneously flowing ($D > D_c$, black disks) active droplets consume ATP at the same rate as samples confined in 100-μm-thick channels (orange disks). Each semitransparent disk represents an active droplet or an active slab confined in a channel. Each dark disk and the error bars represent the mean and the standard deviation of the droplets' speed binned over a 2-μm-diameter interval. The purple line and semitransparent rectangle represent the mean and standard deviation of the ATP-hydrolysis rate measured over all the active droplets.

revealed that both quiescent and flowing active droplets consumed ATP at the same rate as flowing 3D active nematics confined in channels [Fig. 6(g)]. These experiments demonstrated that confinement does not impact the rate at which molecular motors hydrolyze ATP. Finally, we imaged the microtubules at high magnification, which showed that in the quiescent active phase, individual microtubules were still sliding along the nematic director field [Fig. 7(a), Video S6 [53]]. In contrast, in the passive phase, the microtubules were static [Fig. 7(b), Video S6 [53]]. Hence, we concluded that the quiescent active droplets were out-of-equilibrium droplets with active motors that slide microtubules along the nematic director field and not passive droplets with stalled motors. Consequently, the spontaneous flow transition at a finite activity corresponds to the seminal active Fréedericksz transition.

D. Fluctuations in droplet composition induce fluctuations in the emergent flow speed, smoothing the transition close to the bifurcation point

While models of the active Fréedericksz transition predict a sharp transition from a quiescent to a flowing regime, experiments with active droplets display a smooth variation in speed in the vicinity of the transition point [Fig. 2(d), inset]. Further, we also observed the coexistence of quiescent and spontaneously flowing droplets close to

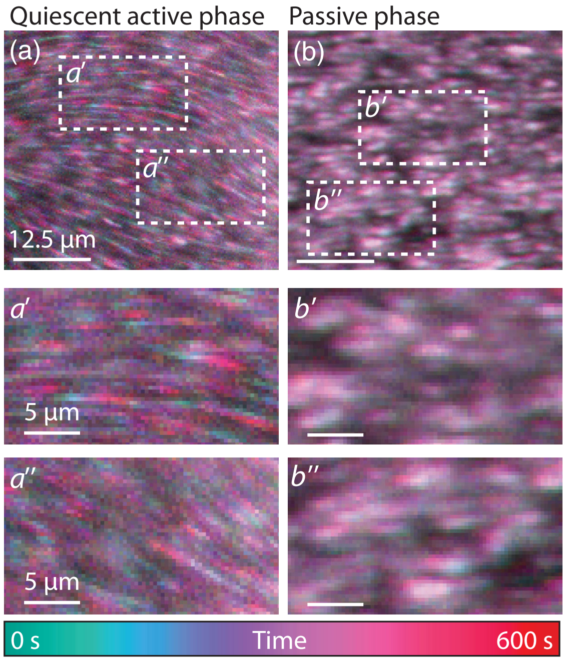

FIG. 7. Microtubules are sliding along bundles in the quiescent active phase. Temporally colored-coded images of microtubules in (a) the quiescent active phase, and (b) the passive phase with no molecular motors. The microtubules are sliding in (a) but are static in (b).

the transition point [Figs. 8(a) and 8(b)]. To explore the origin of this apparent multistability, we performed more experiments with monodisperse active droplets created with a microfluidic droplet generator [55] [Figs. 8(c)–8(g)]. We correlated the speed of each droplet with fluctuations in their composition [Fig. 8(h)]. Flows were measured using PIV and spatially and temporally averaged to get the flow speed. The composition of the droplets was inferred by labeling microtubules, kinesin motor clusters, and fd viruses with distinct fluorophores and simultaneously measuring their fluorescence intensity for each droplet [Figs. 8(d)–8(f)]. We also measured the rate of ATP hydrolysis using the NADH fluorescent sensor [Fig. 8(g)]. The droplets were highly monodisperse ($D = 60.4 \pm 0.5\ \mu\text{m}$, mean ± s.d., $N = 1563$ droplets), and their composition was also tightly distributed. We measured and looked for correlations between speed, size, and composition fluctuations. Droplet size was not correlated with flow speed or with droplet composition [Fig. 8(h), second row and second column]. Flow speed was instead correlated with the concentrations of microtubules, motor clusters, and fd viruses [Fig. 8(h), first row and first column]. However, these three component concentrations were also highly correlated with each other. Motor clusters bind to microtubules; hence, it is not surprising that their fluorescent intensities are proportional to each other, as observed in microtubule-based active isotropic fluids [59]. To isolate the contribution of kinesin-microtubule bundles and viruses on the flow speed, we measured their cross-correlation with flow speed in subsets of active droplets where either the microtubule or fd virus intensities were constant. This was uniquely possible thanks to the large number of active droplets created and imaged at once.

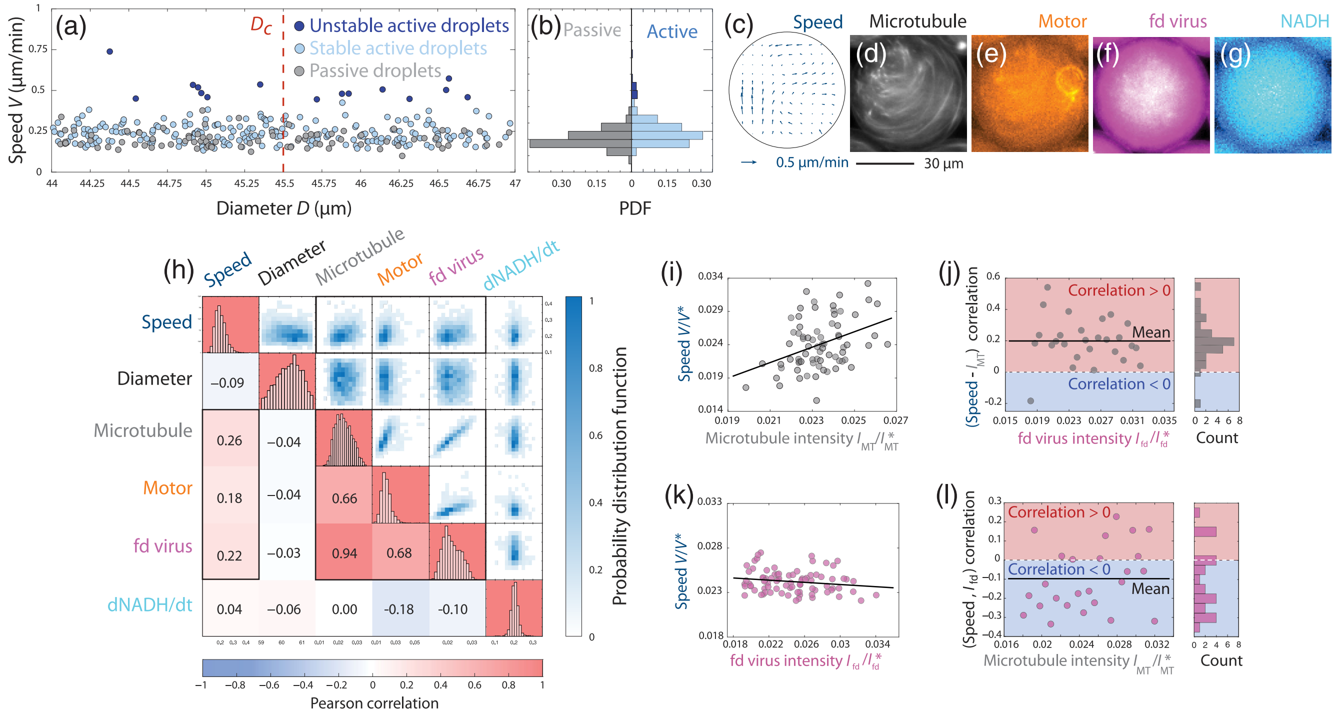

FIG. 8. Fluctuations in droplet composition are responsible for flow speed fluctuations. (a) Plot of flow speed vs diameter in polydisperse active and passive droplets in the vicinity of the critical diameter. We detect the coexistence of spontaneously flowing and quiescent droplets (respectively, in dark and light blue disks). (b) Probability distribution function of the speed of the passive and active droplets over the range of diameters shown in (a). Dark blue bars are statistical outliers in the active sample speed probability distribution function (over 3 standard deviations of the median), which correspond to the spontaneously flowing droplets. (c) Instantaneously flow field and simultaneous fluorescent images of (d) microtubules, (e) motor clusters, (f) fd viruses, and (g) NADH for a single active nematic droplet. (h) Correlation matrix for the speed, diameter, microtubule intensity, motor intensity, fd virus intensity, and ATP-hydrolysis rate over $N = 1563$ monodisperse droplets created with a microfluidic droplet generator. The diagonal shows the probability distribution function of each quantity. The top-right off-diagonals show binned scatter plots of the correlation maps. The bottom-left off-diagonal numbers show the value of the Pearson correlation coefficient. (i) Correlation between flow speed and microtubule intensity at fixed virus intensity. (j) Correlation coefficient between speed and microtubule fluorescent intensity as a function of the virus intensity. Left panel: histogram of the speed-microtubule correlation coefficients for fixed virus intensity. A student *t*-test demonstrates a significant positive correlation (p value $= 8 \times 10^{-8}$, $N = 27$ bins of fd virus intensities). (k) Correlation between flow speed and virus fluorescent intensity at fixed microtubule intensity. (l) Correlation coefficient between speed and virus fluorescent intensity as a function of the microtubule intensity. Left panel: histogram of the speed-virus correlation coefficients for fixed microtubule intensity. A student *t*-test demonstrates a significant negative correlation (p value $= 0.018$, $N = 24$ bins of microtubule intensities).

Figure 8(i) shows that microtubule intensity and speed were positively correlated for fixed fd virus concentrations. A statistical test revealed that the correlation was significantly different from 0 for the range of virus concentrations obtained in the microfluidic droplets [Fig. 8(j)]. Figure 8(k) shows that fd virus intensity and flow speed were negatively correlated for fixed microtubule concentrations. A statistical test revealed that the anticorrelation was significantly different from 0 for the range of microtubule concentrations obtained in the microfluidic droplets [Fig. 8(l)]. These findings are consistent with the fact that active flows are controlled by the kinesin-microtubule bundles and that sample viscosity increases when virus concentration is increased. The fluctuations in flow speed measured in monodisperse droplets result, therefore, from fluctuations in their composition despite being produced from the same active material. Extrapolating these results to polydisperse droplets suggests that the apparent multistability of the active droplets close to the bifurcation point could also result from fluctuations in droplet composition [Figs. 8(a) and 8(b)].

III. DISCUSSION

To summarize, we combined microscopy, simulations, and biochemical assays to understand how hydrodynamic flows spontaneously emerge in confined 3D active nematics. In bulk unconfined nematics, active hydrodynamic flows equally amplify distortions at all length scales [13]. The higher elastic costs associated with short-wavelength modes imply then that long-wavelength deformations are more unstable. Consequently, unconfined homogeneously aligned active nematics are always unstable [13]. However, when confined in channels [16] or droplets, long-wavelength modes are forbidden, and the competition between active and elastic stresses can stabilize a 3D active nematic phase in a quiescent phase despite the finite nonzero activity. Below the critical confinement, the active stress cannot overcome the elastic relaxation and viscous dissipation, and the active liquid crystal confined in droplets lies in a quiescent—yet far-from-equilibrium—state. Biochemical assays that estimate the energy-consumption rate by the molecular motors confirmed that the small quiescent droplets are as active as the larger spontaneously flowing active droplets. These results confirmed that the transition from a quiescent phase to a spontaneously flowing phase in microtubule-based active nematics is the active Fréedericksz transition, theoretically predicted two decades ago [14]. We further showed that the confining geometry can displace the bifurcation point without impacting energy consumption by the motors. Finally, a careful analysis of the flows in active monodisperse droplets revealed that the apparent bistability and the smooth flow transition close to the bifurcation point were due to fluctuations in the droplet's composition. We now consider these findings in the context of previously published results.

First, we wish to compare and contrast the results obtained here with 3D active nematics with the well-characterized 2D active nematics composed of microtubule bundles on an oil-water interface [28,29,34,40,60]. Conceptually, moving from 2D to 3D does not change the nature of the Fréedericksz transition [19]. However, the experiments in 2D and 3D test different limits of the hydrodynamic theory. In many experimental realizations of 2D active nematics, long-range hydrodynamics are screened by interfacial friction: Microtubule bundles are depleted on an oil-water interface [60], bacteria in biofilms swarm on an agar gel [8–11], and mammalian cells adhere to a protein-coated surface [6,61,62]. This is not the case for confined 3D active nematics. The extra third dimension opens the door to future quantitative tests of various active hydrodynamic theoretical predictions. For example, recent work on the dynamics of topological defect lines in spontaneously flowing 3D active nematic confined in droplets [63,64] provides a natural direction to probe how to program emergent structures and flow patterns in 3D liquid crystals, with potential applications for topologically protected information storage [65–67].

Further, our work with a composite active nematic confined in droplets highlights two features that might have precluded the observation of quiescent active phases in other model systems for extensile active nematics. First, the coupling of activity with elasticity in single-component active nematics limits the phase-space exploration. The quiescent phase is found in the high nematic elasticity and low activity regime, which is challenging to reach when the mesogens density sets both activity and nematic elasticity. In single-component microtubule-based liquid crystals, adding diffusive cross-linkers can increase the elasticity of the materials [16], but it also impacts how microtubules assemble into bundles [46] and, therefore, the generation of active stresses. Cross-linking by molecular motors can also increase elasticity, both in microtubule [49] and actin-based [50] active nematics. Here, assembling a composite material where active and passive stresses were independent and tunable alleviated those issues by extending the dimensionality of the design space [42,47]. A similar strategy was used to create "living liquid crystals" where bacteria swim in a passive chromonic liquid crystal, triggering hydrodynamic instabilities and defects nucleation [68–70]. A second important result is the impact of the confining geometry on the active Fréedericksz transition. Stabilizing homogeneously aligned active nematics in channels requires stronger confinement and/or lower activity compared to nonhomogeneously aligned active nematics in droplets. That regime is more challenging to reach experimentally in channels compared to droplets. Another experimental realization of quiescent active nematics in channels was reported for dense 2D monolayers of elongated cells that form a contractile active nematic phase [15].

While active stress is a defining feature of active matter, at the origin of spontaneous flow and other pattern formation, it is unclear how to rationalize its origin from microscopic considerations. In the model system presented here, this difficulty was partially due to the multiscale organization of the motors and microtubules into thick and long extensile bundles [41]. Measuring the magnitude of the active stress and providing a map between molecular composition and emergent properties are important milestones for rationalizing how activity emerges from microscopic energy-consuming building blocks [49,50]. In this study, the small range of experimentally achievable critical diameters ($30\ \mu\mathrm{m} < D_c < 90\ \mu\mathrm{m}$) limits the inference of the magnitude of the active stress or quantitative comparison with theoretical scaling laws. Larger critical diameters could be obtained by decreasing activity. However, at low motor concentrations (below 10 nM), or high fd virus concentration (above 50 mg/mL), the dynamics are slow (approximately 20 μm/h), and the lifetime of the active sample is comparable to the characteristic active timescale (approximately 5 h). Smaller critical diameters could be obtained by increasing activity, for example, by increasing motor concentration. However, in this limit, the critical diameter becomes comparable to the characteristic size of the bundles, and the number of microtubules in each droplet is low. A back-of-the-envelope calculation shows that a 30-μm-diameter droplet contains about 5000 microtubules assembled into even fewer thick bundles. Consequently, the continuum approximation might not be valid in this limit, and hydrodynamic models cannot accurately predict how the system will evolve over time. Similar concerns and discrepancies between experiments and active hydrodynamic models occurred in 2D active nematics confined in small-diameter disks [28].

Here, we provided a quantification of the rate of energy consumption, which might offer new perspectives on energetics, irreversibility, and quantification of how far from equilibrium active materials lie. However, it is still unclear how energy is dissipated at the mesoscopic length scale—between the nanometric scale of the motor step and the macroscopic scale where it is dissipated in spontaneous flows. Combining calorimetry measurements [71,72], multiscale imaging [59], and recent methods from nonequilibrium statistical mechanics and information theory that measure or provide bounds for the rate of entropy production [73–79] might also enrich our understanding of how energy released from ATP hydrolysis propagates through multiple length scales to power dynamical behaviors that are forbidden at equilibrium.

Finally, despite our *in vitro* model system being much simpler than the out-of-equilibrium organelles found in cells, this work might have implications for emergent dynamics in living matter. The mitotic spindle, in particular, is composed of long dynamical microtubules bundled by cross-linkers and various molecular motors. It was successfully modeled as a confined active nematic liquid crystal to explain how the spindle self-organizes during metaphase [12]. Spindles have a similar confining topology as the 3D active nematics droplets studied here. They have an oval shape, with a length varying from around 10 μm for *C. elegans* [80] and mammalian spindles [81] to 50 μm for reconstituted spindles from Xenopus extracts [12] or in zebrafish embryos [82]. Interestingly, the metaphase spindle forms a quiescent active nematic phase, albeit with a nonuniform polarity [12]. Our work showed that strong confinement and low activity can stabilize 3D active nematics. Could larger spindles display spontaneous flows analogous to the 3D microtubule-based active fluids? A similar prediction estimated that spindle in Xenopus extracts with a width larger than 150 μm would be unstable [12]. Future work at the interface of active matter physics and life sciences could shine some light on whether collective deformations in complex 3D living systems can be described using the framework of the active Fréedericksz transition.

ACKNOWLEDGMENTS

We thank Seth Fraden, Colm Kelleher, and Bennett Sessa for fruitful discussions. We thank Shibani Dalal, Director of the Brandeis Biomaterial Facility, for help with protein purification. This work was supported by an NSF CAREER Grant No. DMR-2047119. P. J. F. and A. B. acknowledge support from the Brandeis NSF Materials Research Science and Engineering Center (MRSEC) Grant No. DMR-2011846. H. G. Y. acknowledges support from the National Institute of General Medical Sciences of the National Institutes of Health under Grant No. R00 GM136915. A. B. acknowledges support from Grant No. NSF-DMR-2202353. We also acknowledge the use of the optical, microfluidics, and biomaterial facilities supported by NSF MRSEC Grant No. DMR-2011846. A. S. was funded in part by the Federal Ministry of Education and Research (Bundesministerium für Bildung und Forschung) in the framework of the Center for Scalable Data Analytics and Artificial Intelligence, ScaDS.AI, Dresden and Leipzig. A. S. acknowledges the Scientific Computing Facility of MPI-CBG and the Center for Information Services and High-Performance Computing of TU Dresden for providing the computer resources for the numerical simulations.

APPENDIX A: EXPERIMENTAL MATERIAL AND METHODS

1. Protein and virus purification

a. Microtubules

Tubulin dimers were purified from bovine brains through two cycles of polymerization: depolymerization in high molarity PIPES (1,4- piperazindiethanesulfonic) buffer [83]. Fluorophore-labeled tubulin was prepared by labeling the

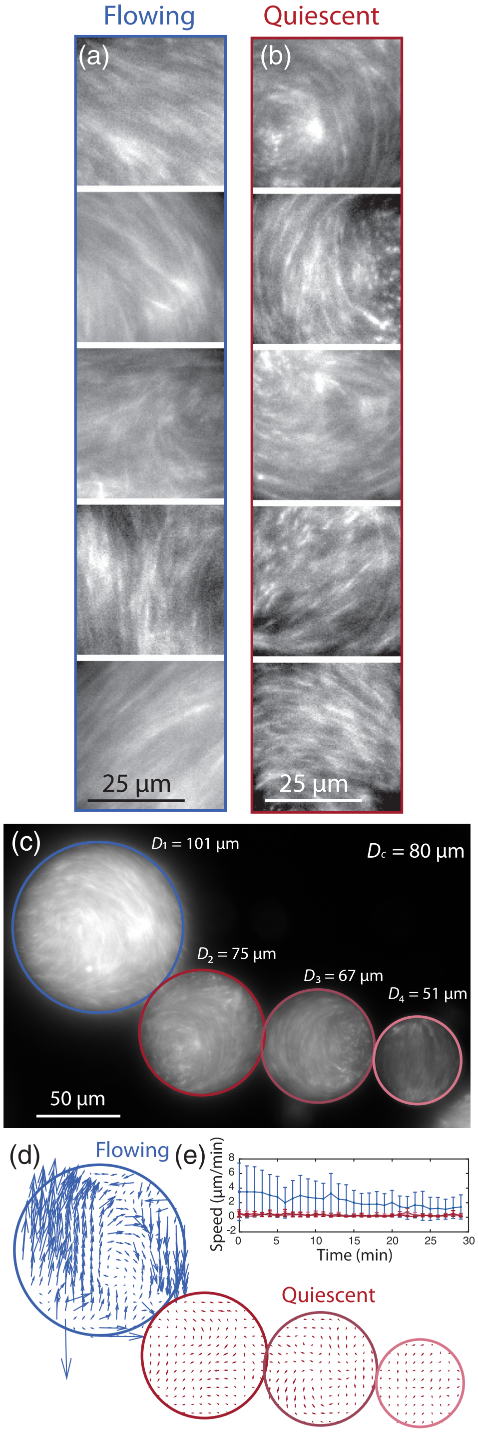

FIG. 9. Kinesin-microtubule bundles have similar morphological features in the quiescent and flowing phases. (a),(b) Enlargement of five distinct droplets with diameters above D_c [(a), flowing droplets] and below D_c [(b), quiescent droplets]. (c) Additional examples of flowing and quiescent droplets with labeled microtubules. The microtubule bundles are continuous, homogeneously distributed throughout the droplets, and locally aligned. (d) Instantaneous flow fields and (e) speed versus time plots confirm which droplets are flowing or quiescent. D_c was measured using the method described in the Appendix A 6.

purified tubulin with Alexa-Fluor 647-NHS (Invitrogen, A-20006) [84]. GMPCPP [guanosine 5’- (α, β methylene-triphosphate)], a nonhydrolyzable analog of GTP was used to stabilize the dynamic instability in the microtubules. The polymerization mixture consisted of 80-μM tubulin (with 3% fluorescently labeled tubulin), 0.6-mM GMPCPP and 1-mM DTT (dithiothreitol) in buffer [80-mM PIPES, 1-mM EGTA (egtazic acid), and 2-mM MgCl2]. After adding all the components, the mixture was incubated at 37 °C for 30 minutes, and subsequently for six hours at room temperature (approximately 20 °C). This method resulted in microtubules of approximately 1.5 μm length on average [34]. The microtubules were aliquoted in small volumes (10 μL), flash frozen in liquid nitrogen, and stored at −80 °C.

b. Kinesin motor clusters and PRC1

K401-BIO-6xHIS (processive motor, dimeric MW-110 kDa) corresponds to the 401 amino acids derived from the *N*-terminal domain of *Drosophila melanogaster* kinesin-1, and labeled with 6-histidine and a biotin tag [85,86]. The motor proteins were transformed and expressed in Rosetta (DE3) pLysS cells and purified following protocols described elsewhere [85]. The purified proteins were flash frozen in liquid nitrogen with 36% sucrose and subsequently stored in −80 °C. We used tetrameric streptavidin (ThermoFisher, 21122, MW: 52.8 kDa) to assemble clusters of biotin-labeled kinesins. To make K401-streptavidin clusters, 5.7 μL of 6.6-μM streptavidin was mixed with 5 μL of 6.4-μM K401 and 0.5 μL of 5-mM DTT in M2B. This mixture was incubated on ice for 30 minutes.

PRC1 was used in the experiment to cross-link microtubules while still allowing the relative sliding by the kinesin motor clusters. PRC1 (MW: 72.5 kDa) was transformed and expressed in Rosetta BL21(DE3) cells, and subsequently purified as previously described [45].

c. Virus purification

Standard biological procedures were followed to grow and purify filamentous fd virus [43] using tetracycline-resistant Phage Display ER2738 as the host *E. coli* strain. Virus samples were stored in M2B buffer. The concentration of the virus was determined using a Nanodrop. Monodispersity was checked using gel electrophoresis. For results shown in Fig. 8, fd viruses were labeled with DyLight488-NHS dye. 5% of the viruses were labeled.

2. Sample preparation

The 3D active nematic was composed of

(i) Alexa 647-labeled GMPCPP stabilized microtubules with an exponential distribution of lengths with an average of 1.5 μm ($[c] = 1.3$ mg/mL). The microtubules are polymerized and stored at −80 °C after flash freezing in liquid nitrogen.

(ii) Multimotor kinesin complexes self-assembled from tetrameric streptavidin and two-headed biotinylated kinesin (K401-Bio) [18] ([motors cluster] = 10–90 nM).

(iii) Microtubule-specific bundling protein, PRC1 (the protein regulator of cytokinesis 1), that passively cross-links antiparallel microtubules, but still allows interfilament sliding [45] ([PRC1] = 200 nM).

(iv) Monodisperse (length approximately 880 nm) fd virus colloidal particles in the nematic phase [43,87]. The fd virus concentration in our experiments ranged from 20 to 50 mg/ml.

(v) ATP with a final concentration of 1420 μM.

(vi) ATP regeneration system: phosphoenol pyruvate (26-mM Phosphoenolpyruvic acid monopotassium salt (PEP), Beantown Chemical, 129745) and pyruvate kinase and lactate dehydrogenase enzymes (2.8% v/v PK/LDH, Sigma, P-0294) [88].

(vii) Antioxidants, an oxygen-scavenging system comprised of glucose (18.7 mM), DTT (5.5 mM), glucose oxidase (1.4 μM), and catalase (0.17 μM) was used to decrease photobleaching.

(viii) M2B buffer: 80-mM PIPES, 2-mM MgCl2, 1-mM EGTA in de-ionized water, *p*H 6.8. The fd, antioxidants, ATP, and PEP were all prepared in this buffer.

The 3D active mixture was finally assembled by mixing viruses and microtubules at the desired concentration and then adding premix (Motor clusters, PRC-1, ATP, ATP regenerating system, antioxidants, and Trolox). To optimize the consistency, a large volume of premix was prepared at one, aliquoted, flash frozen in liquid nitrogen, and stored at −80 °C.

3. Biochemical assays to measure the ATP-hydrolysis rate

a. ATP/NADH-coupled ATPase assay

The ATP regeneration system is essential for rephosphorylating the ADP generated during ATP hydrolysis by kinesin motors, ensuring a consistent ATP concentration. This system involves coupling the pyruvate by-product to a redox reaction downstream, which converts NADH to NAD$^+$. Notably, a single molecule of ATP hydrolysis is coupled to the oxidation of a single molecule of NADH. NADH exhibits fluorescence at a wavelength of 340 nm, while NAD$^+$ has minimal absorption beyond 300 nm [57,89].

(i) We prepared a 15-mM NADH (Sigma-Aldrich) solution in M2B buffer, aliquoted, flash froze, and stored at −80 °C.

(ii) For each experiment, an aliquot of NADH was thawed on ice and incorporated into the premix, resulting in a final concentration of 2.5 mM in the active sample.

(iii) The ATP-hydrolysis rate or NADH oxidation rate was determined by calculating the slope of the fluorescent decrease over time in the sample and comparing its value to the standard curve.

TABLE I. Volumes required for the phosphate standard assay.

Phosphate standard curve reaction			
Phosphate concentration (μM)	0.8-mM phosphate standard volume (μL)	M2B buffer volume (μL)	CytoPhos volume (μL)
0	0	5	195
4	1	4	195
8	2	3	195
12	3	2	195
16	4	1	195
20	5	0	195

The ATP-hydrolysis rate was calculated from the rate of the fluorescence decrease and the known starting concentration of NADH. This rate was compared to a standard curve that showed that fluorescent was proportional to the concentration of NADH. ATP hydrolysis started when caged ATP was exposed to UV light.

In the ATP- and NADH-coupled ATPase assay, antioxidants were omitted from the active samples to prevent interference with the redox reaction that converted NADH to NAD$^+$. This ensured accurate measurement of the ATP-hydrolysis rate or NADH oxidation rate.

b. End-point phosphate assay

ATP underwent hydrolysis, resulting in the formation of ADP and phosphorus as a by-product. We used the CytoPhos Endpoint Phosphate Assay (BK054) kit from Cytoskeleton, Inc. to measure the phosphorus content in

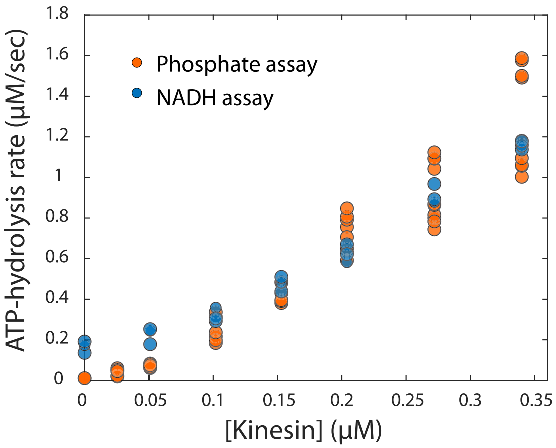

FIG. 10. Comparison of the NADH and phosphate assays. This plot shows the measured ATP-hydrolysis rate for increasing concentrations of kinesin motor clusters. Note the *x* axis shows the concentrations of monomeric kinesin. Multiple independent replicates of the NADH assay (blue disks) and the phosphate assay (orange disks) are shown.

the sample. By determining the total phosphorus amount and the duration of the reaction, the ATP-hydrolysis rate for the sample could be determined. It was based upon a colorimetric change measured at 650 nm, measured with a spectrometer. We used an EPOC 2 plate reader and 96-well plates. The following procedure was employed for this assay:

(i) The lyophilized standard phosphate provided in the kit was reconstituted by adding 125 μL of M2B buffer, resulting in an 800-μM phosphate standard.
(ii) Calibration samples were prepared by adding the phosphate standard to 195 μL of CytoPhos, ensuring a total 200-μL volume in each well. The phosphate concentrations ranged from 0 to 20 μM, as shown in Table I.
(iii) Premix with 1416-μM ATP and required kinesin concentration (0–0.34 μM) was prepared. The components containing phosphates, such as Trolox and PRC-1 protein (stored in a phosphate-containing buffer), were omitted from the premix.
(iv) The reaction was initiated by adding the premix to microtubules after bringing it to room temperature.
(v) After running the reaction for ten minutes, a 5-μL sample was quenched in 195 μL of CytoPhos.
(vi) The quenched mixture was incubated for ten minutes, and a colorimetric measurement was taken.
(vii) The total phosphorus was quantified by mapping the raw optical density measurement of the quenched active sample to the calibration curve obtained from the standard curve.
(viii) The ATP-hydrolysis rate was calculated by dividing the total phosphorus by the run time of the reaction, which was ten minutes.

4. Confining methods

a. Generating polydisperse water-in-oil droplet emulsions of active nematics

In this process, we added 30-50 μL of 2–5 wt% of 008-FluoroSurfactant, a biocompatible surfactant, in HFE7500 fluorinated oil to 12 μL of the sample. Droplets were formed by gently flicking the tube, and the size distribution could be controlled by adjusting the intensity and number of flicks. More flicks resulted in smaller droplets. The droplets were then pipetted into an observation chamber composed of two untreated glass slides and parafilm spacers.

b. Generating monodisperse water-in-oil droplet emulsions

To achieve consistent droplet sizes, we designed and microfabricated a microfluidic drop-maker device [55]. The same fluorinated oil and surfactant were used to produce polydisperse droplets. Droplet size was controlled by adjusting the sample-oil flow rates and the dimensions of the nozzle, where the pinching effect by oil generates the droplets. The nozzle size ranged from 20 to 50 μm. We used syringe pumps to regulate the sample and oil flow rates. The flow rate for the oil phase was set to 1000-μL/h, and the flow rate of the active sample was set to 100–200 μL/h, which prevented jetting. To prevent protein adhesion to the microfluidic device and tubings, we incubated them with a 2.5% pluronic solution and 45-mg/ml BSA for five minutes. The droplets were then pipetted into an observation chamber composed of two untreated glass slides and parafilm spacers.

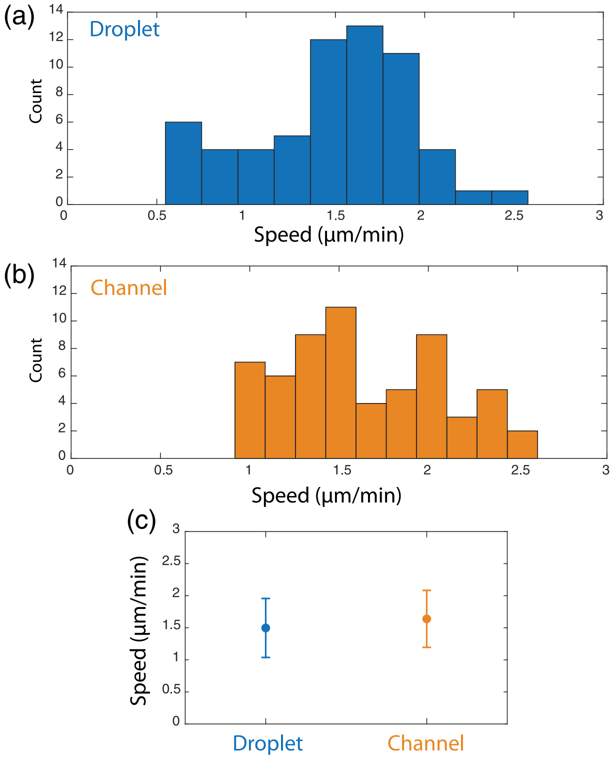

FIG. 11. Comparison of speed in channels and in droplets. (a) Speed distribution in a 100-μm-diameter droplet. (b) Speed distribution in a 100-μm-thick channel. (c) Comparison of the mean and standard deviation between the speed distributions in droplets and channels. $[\mathrm{ATP}] = 1.4$ mM, $[\mathrm{microtubule}] = 1.3$ mg/mL, $[\mathrm{motor clusters}] = 30$ nM, $[\mathrm{fd\ virus}] = 40$ mg/mL.

c. Channels

All flow chambers were assembled using two glass slides spaced by a layer of parafilm (height = 100 μm, width = 3 mm). The glass surfaces were coated with an acrylamide brush to prevent nonspecific protein adsorption [18]. Parafilm spacers were cut and placed between the two glass surfaces followed by a mild heat treatment at 60 °C to melt the parafilm so it could bind to the glass surfaces. The active mixture was loaded into each channel type by capillarity and sealed with a UV-curing optical adhesive (NOA 81, Norland Products Inc.).

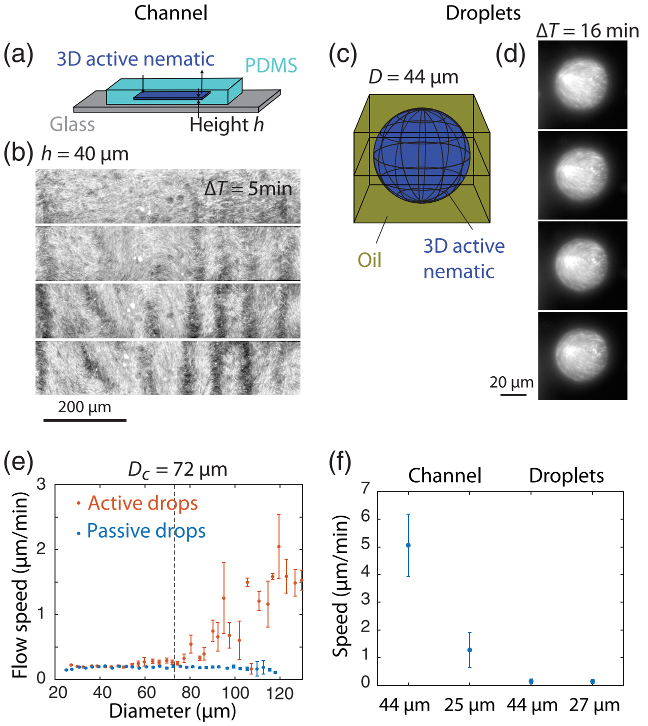

FIG. 12. Experimental comparison of channel and droplet geometry. (a) Schematic of the experiment performed in channels. (b) Fluorescent images of a 3D active nematic confined in a channel of thickness 40 μm. Time series shows a picture every five minutes. The homogeneously aligned nematic phase is unstable and starts to flow and deform spontaneously. (c) Schematic of the experiment performed in water-in-oil emulsion. (d) Fluorescent images of a 3D active nematic confined in a droplet of 40-μm diameter. Time series shows a picture every 16 minutes. The active droplet is quiescent. (e) Speed vs diameter plot shows for active and passive droplets. The critical diameter is around 72 μm. (f) Speed comparison of the same 3D active nematics confined in channels of height 44 and 25 μm or in droplets of 44- and 25-μm diameter. $[\mathrm{ATP}] = 1.4$ mM, $[\text{motor clusters}] = 30$ nM, $[\text{fd virus}] = 40$ mg/mL.

5. Microscopy

a. Widefield fluorescence microscopy

Time-lapse image acquisitions were taken using a Nikon Eclipse Ti2 inverted fluorescent microscope with an XYZ position control equipped with an LED light source (Lumencor sola 80-10244). The mutiposition data acquisitions, the time interval between the images, exposure time, and illumination power were controlled by micromanager [90]. The typical delay between two successive images of the same field of view was set to be 30–90 s depending on the speed of the active sample, ensuring good time resolution for accurate PIV. That delay was kept the same for different samples in the same experiment. A Hamamatsu camera (ORCA4.0V1, pixel size 6.45 μm) and a 20 × objective (Nikon Plan Apo) were used for imaging the droplets experiments.

b. Confocal microscopy

We used confocal microscopy to image slices of the 3D active nematics confined in droplets. The experiment was performed on an inverted microscope (Nikon, Ti2 Eclipse) equipped with spinning disk module (CrestoOptics, X-Light V2) and an automated XY stage (ASI MS2000). Fluorescent microtubules were illuminated with the appropriate excitation wavelength from a light source (Lumencor, CELESTA light engine). A Hamamatsu camera (ORCA4.0V1) and a 20 × objective (Nikon Apo LWD) was used for imaging the samples. The step size was set to 0.86 μm.

6. Analysis

a. Image analysis and flow measurement

The velocity field was mapped by PIV analysis on microtubule bundles. A time series of images within the field of view was subjected to PIV analysis using PIVlab based on the MatPIV software package from MathWorks [91]. The PIV analysis utilized a window size of 32 pixels (equivalent to 10.4 μm) with 75% overlap. We developed an automated image analysis pipeline to segment the droplets. Fluorescent images were first flattened to remove any uneven illumination patterns on the edges. Droplets touching an edge were removed. Image stacks were time averaged to segment only circular droplets that were immobile. Mobile droplets appeared noncircular and were removed from further analysis. Circular droplets were detected using a circular Hough transform. A binary mask was created for each segmented droplet and superimposed on the PIV flow field to isolate the contribution of each droplet to the flows. Flows were then spatially and temporally averaged over 60 minutes.

b. Determining critical diameter by statistical t-test

We used the MATLAB function “ttest2(x,y,‘Tail’,‘right’)” to perform a two-sample t-test and compared the speed distributions of active and passive droplets. This statistical test determined whether the mean of one group “x” was significantly higher than the other independent group “y.” Here, the test group x was the flow speed data of active drops, and the control group y was passive drops for given diameter (usually 3-μm bin interval). When there was no flow or flow suppression in active droplets, the t-test showed no significant difference compared to passive droplets, with p values above 0.05. However, there was a clear distinction for the flowing state, with p values below 0.05. The critical diameter marked the diameter above which p values started to show statistical significance. Often, the flow-to-no-flow transition is not smooth, and the p value fluctuates between high and low. The critical diameter is confirmed if the p value remains continuously significant above the determined critical diameter up to the set threshold (usually 10 μm).

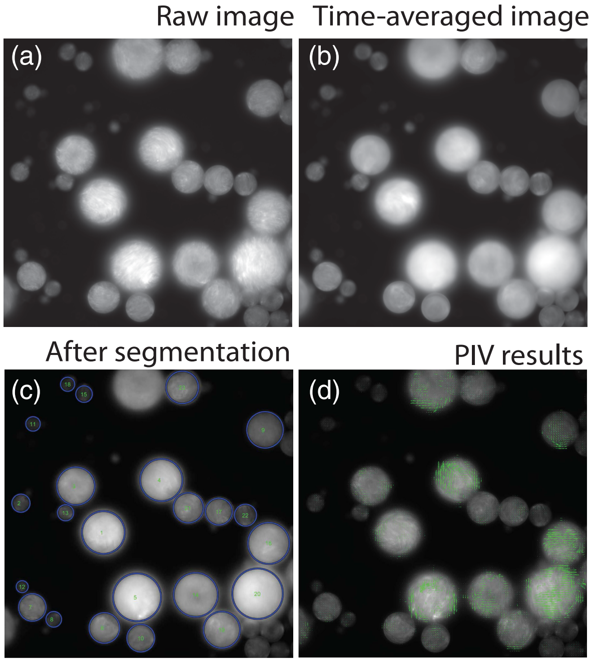

FIG. 13. Image analysis pipeline to segment and measure flows in droplets. (a) Fluorescent image of the 3D active nematic droplets. $[\text{ATP}] = 1.42$ mM, $[\text{motor clusters}] = 40$ nM, $[\text{fd virus}] = 45$ mg/mL. (b) Time-averaged image over 60 minutes. Droplets that move through the field of view appear noncircular. (c) Result of the segmentation. Droplets that are not circular or that touch an edge are removed. (d) Flow field from PIV. All four fields of view are 660 by 660 μm.

APPENDIX B: THEORETICAL MODEL

To demonstrate that confinement in droplets can stabilize 3D active nematics, we performed nonlinear numerical simulations of a symmetry-preserving active Ericksen-Leslie hydrodynamic model. This model, previously developed to study the Fréedericksz transition in 3D active nematics confined between two parallel plates [19], extended to 3D the results of the seminal model of 2D active polar fluids [14]. In 3D channels, the critical confinement L_c scales as $\sqrt{K/\Delta\mu}$ where $\Delta\mu$ is the active potential that is proportional to the magnitude of the active stress, and K is the nematic elasticity. Below that critical confinement, the 3D active nematic stays in a quiescent homogeneously aligned active phase. Here, we extended this model to study how spherical confinement impacted the active Fréedericksz transition.

The temporal evolution of the polarity vector field $\mathbf{p}$ is dictated by

$$\frac{\partial p_\alpha}{\partial t} + v_\gamma \partial_\gamma p_\alpha + \omega_{\alpha\beta} p_\beta = \frac{h_\alpha}{\gamma} - \nu u_{\alpha\beta} p_\beta + \lambda \Delta\mu p_\alpha, \tag{B1}$$

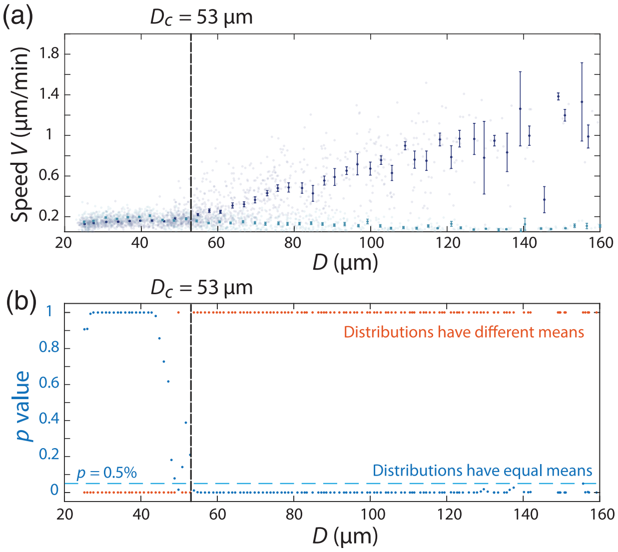

FIG. 14. Results of a one-sided statistical test comparing flow speed distributions in passive (without motor clusters) and active droplets. (a) Plot of the speed vs droplet diameter for active (dark blue) and passive droplets (light blue). (b) Results of the statistical analysis. The p value is shown in blue, and the binary result from the test is in red. The critical diameter is chosen when the active and passive distributions have different means.

where $u_{\alpha\beta} = \frac{1}{2}(\partial_\alpha v_\beta + \partial_\beta v_\alpha)$ is the strain-rate tensor, and $\omega_{\alpha\beta} = \frac{1}{2}(\partial_\alpha v_\beta - \partial_\beta v_\alpha)$ is the vorticity tensor. Ensuring the conservation of momentum in the fluid, we have

$$\partial_\beta \sigma_{\alpha\beta}^{(\mathrm{tot})} - \partial_\alpha \Pi = 0, \tag{B2}$$

along with the incompressibility condition

$$\partial_\gamma v_\gamma = 0. \tag{B3}$$

The constitutive relation between the strain-rate tensor $u_{\alpha\beta} = \frac{1}{2}(\partial_\alpha v_\beta + \partial_\beta v_\alpha)$, and the active stress tensor σ is as follows:

$$\begin{aligned} 2\eta u_{\alpha\beta} = \sigma_{\alpha\beta}^{(s)} + \zeta \Delta\mu \left(p_\alpha p_\beta - \frac{1}{3} p_\gamma p_\gamma \delta_{\alpha\beta} \right) \\ - \frac{\nu}{2} \left(p_\alpha h_\beta + p_\beta h_\alpha - \frac{2}{3} p_\gamma h_\gamma \delta_{\alpha\beta} \right), \end{aligned} \tag{B4}$$

where $\zeta = 1$ represents extensile stress for the active potential $\Delta\mu > 0$, ν is the flow alignment parameter, λ couples the polarity to the active potential $\Delta\mu$, and γ is the rotational viscosity.

The molecular field (h) can be decomposed into parallel and perpendicular components as follows: Parallel component

$$h_{\parallel} = \mathbf{p} \cdot \mathbf{h} = p_x h_x + p_y h_y + p_z h_z. \tag{B5}$$

Perpendicular component

$$\begin{aligned}\mathbf{h}_{\perp} = \mathbf{p} \times \mathbf{h} &= (h_{\perp x}, h_{\perp y}, h_{\perp z}) \\ &= (p_y h_z - p_z h_y, p_z h_x - p_x h_z, p_x h_y - p_y h_x).\end{aligned} \tag{B6}$$

The vector $\mathbf{h}_{\perp}$ is calculated from the variational derivative of the Frank free-energy density:

$$\begin{aligned}F_{3\mathrm{D}} = {}& \frac{K_s}{2}(\nabla \cdot \mathbf{p})^2 + \frac{K_t}{2}(\mathbf{p} \cdot \nabla \times \mathbf{p})^2 \\ & + \frac{K_b}{2}[\mathbf{p} \times (\nabla \times \mathbf{p})]^2 - \frac{1}{2} h_{\parallel}^0 \|\mathbf{p}\|^2.\end{aligned} \tag{B7}$$

The total stress $\sigma_{\alpha\beta}^{(\mathrm{tot})}$ is decomposed into symmetric, antisymmetric, and equilibrium stresses. The equilibrium stress, also called the Ericksen stress, is given by

$$\sigma_{\alpha\beta}^{(\mathrm{e})} = -\frac{\partial F_{3\mathrm{D}}}{\partial(\partial_\beta p_\gamma)} \partial_\alpha p_\gamma. \tag{B8}$$

The antisymmetric stress is

$$\sigma_{\alpha\beta}^{(\mathrm{ant})} = \frac{1}{2}(p_\alpha h_\beta - p_\beta h_\alpha). \tag{B9}$$

The Lagrange multiplier to maintain constant polarity magnitude is given by [19,92]

$$\begin{aligned}h_{\parallel}^0 = h_{\parallel} = -\gamma \Bigg[& \lambda \Delta\mu - \frac{\nu}{p_x^2 + p_y^2 + p_z^2}(u_{xx} p_x^2 \\ & + u_{yy} p_y^2 + u_{zz} p_z^2 + 2u_{xy} p_x p_y \\ & + 2u_{yz} p_y p_z + 2u_{xz} p_x p_z)\Bigg].\end{aligned} \tag{B10}$$

We can substitute the decomposition of $\mathbf{h}$ as follows:

$$h_x = h_{\parallel} p_x - h_{\perp z} p_y + h_{\perp z} p_y, \tag{B11a}$$

$$h_y = h_{\parallel} p_y + h_{\perp z} p_x - h_{\perp x} p_z, \tag{B11b}$$

$$h_z = h_{\parallel} p_z + h_{\perp x} p_y - h_{\perp y} p_x. \tag{B11c}$$

1. Numerical implementation

We fix polarity at the boundary with Dirichlet boundary conditions using vector spherical harmonics,

$$\mathbf{p} = \sum_{l=0}^{l_{\max}} \sum_{m=-l}^{l} u_{lm}^r(r) \mathbf{Y}^{(lm)} + u_{lm}^{(1)}(r) \mathbf{\Psi}^{(lm)} + u_{lm}^{(2)}(r) \mathbf{\Phi}^{(lm)}, \tag{B12}$$

where $\mathbf{Y}^{(lm)}$, $\mathbf{\Psi}^{(lm)}$, and $\mathbf{\Phi}^{(lm)}$ are the vector spherical harmonics. We choose $l_{\max} = 2$, $u_{10}^r(r) = 1$, and the rest of the coefficients are 0. This leads to a 2D order field on the surface of the sphere with two asters located at the poles of the sphere in the chosen coordinate system and a vector field aligned with the z direction in the center of the sphere.

The steady-state Stokes flow equations derived from the force-balance equation [Eq. (B2)] and the Lagrange multiplier from Eq. (B10) were implemented into a computational program using a custom C++ expression system [93] within the scalable OpenFPM scientific computing library [94]. Spatial derivatives were discretized on point clouds with a spherical boundary using the discretization-corrected particle strength exchange scheme [95].

In the initial condition, the polarity was uniformly aligned with the anchoring Dirichlet boundary condition on the surface using vector spherical harmonics as described in the previous section. We introduced a small perturbation of 0.01 rad in the positive X and Y directions at the center of the sphere ($r < 2 \times \text{spacing}$) introduced to break the symmetry.

The evolution of polarity over time was calculated using the Adams-Bashforth-Moulton predictor-corrector time-integration method with a time step of 0.01 and slope renormalization, until final time $t_f = 400$. The velocity field was calculated through an iterative correction of pressure and solving the implicit system of incompressible Ericksen-Leslie Stokes equations with hydrodynamic no-slip boundary conditions at the surface of the sphere. Each time step's resultant linear system of equations was numerically solved using the iterative GMRES solver in the PETSc software library [96]. Our checks using higher resolutions confirmed grid convergence, as the same results were achieved. Additional numerical and computer code details can be found in Ref. [92]. The critical diameter was determined by interpolating the numerically obtained flow velocity at $t = 100$ for various diameters using the monotonic cubic interpolation (PchipInterpolator from SCIPY) and finding the diameter for which the flow velocities exceeded a threshold value of 0.09.

2. Simulation results

We simulated the 3D active nematics in droplets of increasing diameter D. The simulation results confirmed that 3D active nematics in droplets were quiescent below a critical diameter despite being nonhomogeneously aligned [Fig. 4(a), Video S3 [53]]. Below the critical diameter, the magnitude of the flow vectors numerically approached zero. The flow magnitude converged to zero with increasing resolution in space and time. Above that diameter, active droplets started to spontaneously flow [Figs. 4(b) and 4(c), Video S3 [53]]. Above the transition point, the steady-state flow speed increased with the droplet's diameter [Fig. 4(d)]. The critical diameter decreased when activity was increased [Fig. 4(d), inset] or when nematic elasticity was decreased

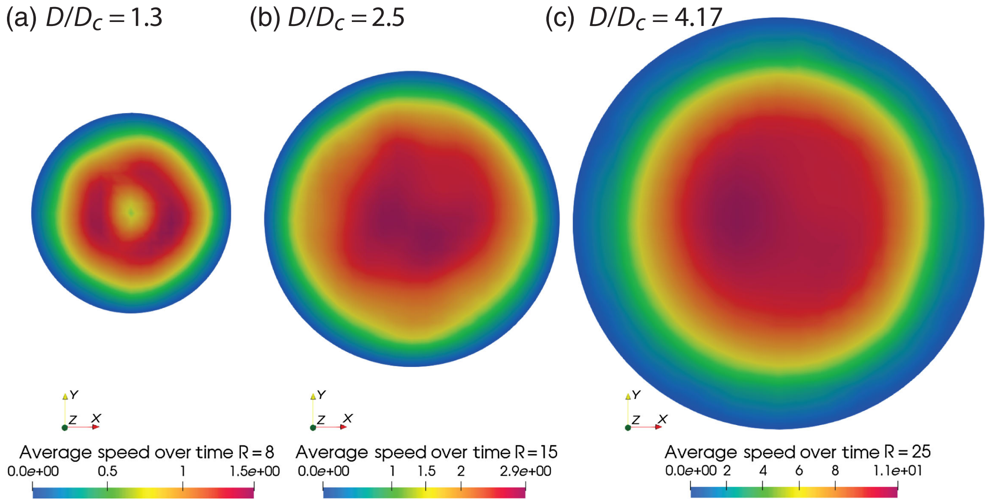

FIG. 15. Simulation results for time-averaged rms speed in spontaneously flowing droplets. (a) $D/D_c = 1.3$, (b) $D/D_c = 2.5$, and (c) $D/D_c = 4.17$. The parameters used are $L_a = \sqrt{0.3} = 0.548$, $K = 1.5$, $\Delta\mu = 5$, $\zeta = 1$, $\gamma = 1$, $\eta = 1$, $\lambda = 0$, $\nu = -1$.

[Fig. 4(e), inset]. Simulation results showed that the critical diameter scaled linearly with the active length scale $\sqrt{K/\Delta\mu}$ [Fig. 4(e)], which was the same scaling as in channels geometry [Fig. 4(e), dashed line] [19].

3. Expression for critical activity in channels

The analytical expression for the critical activity in a 3D channel for tangential anchoring on the walls and extensile active stress is known from Ref. [19] as

$$\Delta\mu_c = -(\alpha)\frac{K(\gamma(\nu-1)^2+4\eta)}{2\gamma(\nu-1)L^2(\gamma\lambda\nu+\zeta)} \tag{B13}$$

with the prefactor $\alpha = 4\pi^2$ and confining length L.

We make the equations dimensionless with respect to ζ, η, thereby defining an active timescale $t_a = (1/\Delta\mu)$, and the active length scale $l_a = \sqrt{K/\Delta\mu}$.

Our numerical simulations demonstrate that the prefactor α is larger for spherical confinement compared to confinement in channels [Fig. 4(e)]. Therefore, for similar confinement, the critical activity is lower for a homogeneously aligned phase confined in channels compared to a distorted phase confined in spherical droplets.

APPENDIX C: SUPPLEMENTAL VIDEO CAPTIONS

(i) *Video S1:* Spontaneously flowing active nematic confined in a large droplet ($D = 180$ μm) Confocal microscopy video taken in the droplet midplane. Microtubules are labeled. [Motor cluster] = 30 nM, [ATP] = 1.4 mM, [fd] = 40 mg/mL.

(ii) *Video S2:* Polydisperse active nematic droplets. Widefield fluorescence microscopy video taken with a 20 × objective. [Motor cluster] = 30 nM, [ATP] = 1.4 mM, [fd] = 45 mg/mL.

(iii) *Video S3:* Simulation of active nematic droplet. Numerical simulations of the active Erickson-Leslie hydrodynamical model performed using the OpenFPM library. The first panel shows the orientation field color coded as a function of the Frank energy density for a quiescent active droplet. The second panel shows the orientation field color coded as a function of the Frank energy density for a spontaneously flowing active droplet. The left panel shows the flow field color coded as a function of the flow speed for the same droplet as in the middle panel. The parameters used are $L_a = \sqrt{0.3} = 0.548$, $K = 1.5$, $\Delta\mu = 5$, $\zeta = 1$, $\gamma = 1$, $\eta = 1$, $\lambda = 0$, $\nu = -1$. Radius = 4 for the left panel, radius = 8 for the middle and right panels.

(iv) *Video S4:* Active Fréedericksz transition *in silico*. Active droplet starts in the quiescent phase ($\Delta\mu = 2$). After 200 time steps, activity is increased to $\Delta\mu = 5$, and the droplet starts to flow. The parameters used are $L_a = \sqrt{0.3} = 0.548$, $K = 1.5$, $\zeta = 1$, $\gamma = 1$, $\eta = 1$, $\lambda = 0$, $\nu = -1$.

(v) *Video S5:* Bend instability in a 3D active nematic confined in a thin channel. Height = 40 μm, width = 3 mm. When the active phase is confined in droplets of similar size, the droplets are in the quiescent active phase. [ATP] = 1.4 mM, [motor clusters] = 30 nM, [fd virus] = 40 mg/mL.

(vi) *Video S6:* Representative videos of the quiescent active phase (left [motor clusters] = 30 nM, D = 61 m) and the passive phase (right, no molecular motors, $D = 134$ μm). [ATP] = 1.4 mM, [fd virus] = 40 mg/mL.

[1] A. Doostmohammadi, J. Ignes-Mullol, J. M. Yeomans, and F. Sagues, *Active nematics*, Nat. Commun. **9**, 3246 (2018).

[2] S. Shankar, A. Souslov, M. J. Bowick, M. C. Marchetti, and V. Vitelli, *Topological active matter*, Nat. Rev. Phys. **4**, 380 (2022).

[3] M. J. Bowick, N. Fakhri, M. C. Marchetti, and S. Ramaswamy, *Symmetry, thermodynamics, and topology in active matter*, Phys. Rev. X **12**, 010501 (2022).

[4] V. Narayan, S. Ramaswamy, and N. Menon, *Long-lived giant number fluctuations in a swarming granular nematic*, Science **317**, 105 (2007).

[5] K. Kawaguchi, R. Kageyama, and M. Sano, *Topological defects control collective dynamics in neural progenitor cell cultures*, Nature (London) **545**, 327 (2017).

[6] T. B. Saw, A. Doostmohammadi, V. Nier, L. Kocgozlu, S. Thampi, Y. Toyama, P. Marcq, C. T. Lim, J. M. Yeomans, and B. Ladoux, *Topological defects in epithelia govern cell death and extrusion*, Nature (London) **544**, 212 (2017).

[7] G. Duclos, S. Garcia, H. G. Yevick, and P. Silberzan, *Perfect nematic order in confined monolayers of spindle-shaped cells*, Soft Matter **10**, 2346 (2014).

[8] J. Nijjer, M. Kothari, C. Li, T. Henzel, Q. Zhang, J. B. Tai, S. Zhou, S. Zhang, T. Cohen, and J. Yan, *Biofilms as self-shaping growing nematics*, Nat. Phys. **19**, 1936 (2023).

[9] Y. I. Yaman, E. Demir, R. Vetter, and A. Kocabas, *Emergence of active nematics in chaining bacterial biofilms*, Nat. Commun. **10**, 2285 (2019).

[10] R. Hartmann, P. K. Singh, P. Pearce, R. Mok, B. Song, F. Diaz-Pascual, J. Dunkel, and K. Drescher, *Emergence of three-dimensional order and structure in growing biofilms*, Nat. Phys. **15**, 251 (2019).

[11] K. Copenhagen, R. Alert, N. S. Wingreen, and J. W. Shaevitz, *Topological defects promote layer formation in myxococcus xanthus colonies*, Nat. Phys. **17**, 211 (2020).

[12] J. Brugues and D. Needleman, *Physical basis of spindle self-organization*, Proc. Natl. Acad. Sci. U.S.A. **111**, 18496 (2014).

[13] R. A. Simha and S. Ramaswamy, *Hydrodynamic fluctuations and instabilities in ordered suspensions of self-propelled particles*, Phys. Rev. Lett. **89**, 058101 (2002).

[14] R. Voituriez, J.-F. Joanny, and J. Prost, *Spontaneous flow transition in active polar gels*, Europhys. Lett. **70**, 404 (2005).

[15] G. Duclos, C. Blanch-Mercader, V. Yashunsky, G. Salbreux, J. F. Joanny, J. Prost, and P. Silberzan, *Spontaneous shear flow in confined cellular nematics*, Nat. Phys. **14**, 728 (2018).

[16] P. Chandrakar, M. Varghese, S. A. Aghvami, A. Baskaran, Z. Dogic, and G. Duclos, *Confinement controls the bend instability of three-dimensional active liquid crystals*, Phys. Rev. Lett. **125**, 257801 (2020).

[17] S. Ramaswamy and M. Rao, *Active-filament hydrodynamics: Instabilities, boundary conditions and rheology*, New J. Phys. **9**, 423 (2007).

[18] T. Sanchez, D. T. Chen, S. J. DeCamp, M. Heymann, and Z. Dogic, *Spontaneous motion in hierarchically assembled active matter*, Nature (London) **491**, 431 (2012).

[19] A. Singh, Q. Vagne, F. Jülicher, and I. F. Sbalzarini, *Spontaneous flow instabilities of active polar fluids in three dimensions*, Phys. Rev. Res. **5**, L022061 (2023).

[20] V. Fréedericksz and A. Repiewa, *Theoretisches und experimentelles zur frage nach der natur der anisotropen flüssigkeiten*, Z. Phys. **42**, 532 (1927).

[21] V. Fréedericksz and V. Zolina, *Forces causing the orientation of an anisotropic liquid*, Trans. Faraday Soc. **29**, 919 (1933).

[22] K.-T. Wu, J. B. Hishamunda, D. T. Chen, S. J. DeCamp, Y.-W. Chang, A. Fernández-Nieves, S. Fraden, and Z. Dogic, *Transition from turbulent to coherent flows in confined three-dimensional active fluids*, Science **355**, eaal1979 (2017).

[23] H. Wioland, F. G. Woodhouse, J. Dunkel, J. O. Kessler, and R. E. Goldstein, *Confinement stabilizes a bacterial suspension into a spiral vortex*, Phys. Rev. Lett. **110**, 268102 (2013).

[24] E. Lushi, H. Wioland, and R. E. Goldstein, *Fluid flows created by swimming bacteria drive self-organization in confined suspensions*, Proc. Natl. Acad. Sci. U.S.A. **111**, 9733 (2014).

[25] M. Ravnik and J. M. Yeomans, *Confined active nematic flow in cylindrical capillaries*, Phys. Rev. Lett. **110**, 026001 (2013).

[26] M. Varghese, A. Baskaran, M. F. Hagan, and A. Baskaran, *Confinement-induced self-pumping in 3D active fluids*, Phys. Rev. Lett. **125**, 268003 (2020).

[27] S. Chandragiri, A. Doostmohammadi, J. M. Yeomans, and S. P. Thampi, *Flow states and transitions of an active nematic in a three-dimensional channel*, Phys. Rev. Lett. **125**, 148002 (2020).

[28] A. Opathalage, M. M. Norton, M. P. Juniper, B. Langeslay, S. A. Aghvami, S. Fraden, and Z. Dogic, *Self-organized dynamics and the transition to turbulence of confined active nematics*, Proc. Natl. Acad. Sci. U.S.A. **116**, 4788 (2019).

[29] J. Hardoüin, R. Hughes, A. Doostmohammadi, J. Laurent, T. Lopez-Leon, J. M. Yeomans, J. Ignés-Mullol, and F. Sagués, *Reconfigurable flows and defect landscape of confined active nematics*, Commun. Phys. **2**, 121 (2019).

[30] T. N. Shendruk, A. Doostmohammadi, K. Thijssen, and J. M. Yeomans, *Dancing disclinations in confined active nematics*, Soft Matter **13**, 3853 (2017).

[31] A. Mozaffari, R. Zhang, N. Atzin, and J. J. de Pablo, *Defect spirograph: Dynamical behavior of defects in spatially patterned active nematics*, Phys. Rev. Lett. **126**, 227801 (2021).

[32] C. G. Wagner, M. M. Norton, J. S. Park, and P. Grover, *Exact coherent structures and phase space geometry of preturbulent 2D active nematic channel flow*, Phys. Rev. Lett. **128**, 028003 (2022).

[33] F. Mori, S. Bhattacharyya, J. M. Yeomans, and S. P. Thampi, *Viscoelastic confinement induces periodic flow reversals in active nematics*, Phys. Rev. E **108**, 064611 (2023).

[34] S. J. DeCamp, G. S. Redner, A. Baskaran, M. F. Hagan, and Z. Dogic, *Orientational order of motile defects in active nematics*, Nat. Mater. **14**, 1110 (2015).

[35] N. Kumar, R. Zhang, J. J. d. Pablo, and M. L. Gardel, *Tunable structure and dynamics of active liquid crystals*, Sci. Adv. **4**, eaat7779 (2018).

[36] A. J. Tan, E. Roberts, S. A. Smith, U. A. Olvera, J. Arteaga, S. Fortini, K. A. Mitchell, and L. S. Hirst, *Topological chaos in active nematics*, Nat. Phys. **15**, 1033 (2019).

[37] L. M. Lemma, S. J. DeCamp, Z. You, L. Giomi, and Z. Dogic, *Statistical properties of autonomous flows in 2D active nematics*, Soft Matter **15**, 3264 (2019).

[38] L. M. Lemma, M. Varghese, T. D. Ross, M. Thomson, A. Baskaran, and Z. Dogic, *Spatiotemporal patterning of extensile active stresses in microtubule-based active fluids*, Proc. Natl. Acad. Sci. U.S.A. **2**, pgad130 (2023).

[39] P. Guillamat, J. Ignes-Mullol, and F. Sagues, *Taming active turbulence with patterned soft interfaces*, Nat. Commun. **8**, 564 (2017).

[40] B. Martínez-Prat, R. Alert, F. Meng, J. Ignés-Mullol, J.-F. Joanny, J. Casademunt, R. Golestanian, and F. Sagués, *Scaling regimes of active turbulence with external dissipation*, Phys. Rev. X **11**, 031065 (2021).

[41] B. Lemma, L. M. Lemma, S. C. Ems-McClung, C. E. Walczak, Z. Dogic, and D. J. Needleman, *Structure and dynamics of motor-driven microtubule bundles*, Soft Matter **20**, 5715 (2024).

[42] G. Duclos, R. Adkins, D. Banerjee, M. S. E. Peterson, M. Varghese, I. Kolvin, A. Baskaran, R. A. Pelcovits, T. R. Powers, A. Baskaran, F. Toschi, M. F. Hagan, S. J. Streichan, V. Vitelli, D. A. Beller, and Z. Dogic, *Topological structure and dynamics of three-dimensional active nematics*, Science **367**, 1120 (2020).

[43] Z. Dogic and S. Fraden, *Cholesteric phase in virus suspensions*, Langmuir **16**, 7820 (2000).

[44] P. Bieling, I. A. Telley, and T. Surrey, *A minimal midzone protein module controls formation and length of antiparallel microtubule overlaps*, Cell **142**, 420 (2010).

[45] R. Subramanian, E. M. Wilson-Kubalek, C. P. Arthur, M. J. Bick, E. A. Campbell, S. A. Darst, R. A. Milligan, and T. M. Kapoor, *Insights into antiparallel microtubule crosslinking by PRC1, a conserved nonmotor microtubule binding protein*, Cell **142**, 433 (2010).

[46] P. Chandrakar, J. Berezney, B. Lemma, B. Hishamunda, A. Berry, K. T. Wu, R. Subramanian, J. Chung, D. Needleman, J. Gelles, and Z. Dogic, *Engineering stability, longevity, and miscibility of microtubule-based active fluids*, Soft Matter **18**, 1825 (2022).

[47] J. Berezney, B. L. Goode, S. Fraden, and Z. Dogic, *Extensile to contractile transition in active microtubule-actin composites generates layered asters with programmable lifetimes*, Proc. Natl. Acad. Sci. U.S.A. **119**, e2115895119 (2022).

[48] R. Adkins, I. Kolvin, Z. You, S. Witthaus, M. C. Marchetti, and Z. Dogic, *Dynamics of active liquid interfaces*, Science **377**, 768 (2022).

[49] B. Najma, M. Varghese, L. Tsidilkovski, L. Lemma, A. Baskaran, and G. Duclos, *Competing instabilities reveal how to rationally design and control active crosslinked gels*, Nat. Commun. **13**, 6465 (2022).

[50] S. A. Redford, J. Colen, J. L. Shivers, S. Zemsky, M. Molaei, C. Floyd, P. V. Ruijgrok, V. Vitelli, Z. Bryant, A. R. Dinner, and M. L. Gardel, *Motor crosslinking augments elasticity in active nematics*, Soft Matter **20**, 2480 (2024).

[51] D. A. Gagnon, C. Dessi, J. P. Berezney, R. Boros, Daniel T.-N. Chen, Z. Dogic, and D. L. Blair, *Shear-induced gelation of self-yielding active networks*, Phys. Rev. Lett. **125**, 178003 (2020).

[52] K. Visscher, M. J. Schnitzer, and S. M. Block, *Single kinesin molecules studied with a molecular force clamp*, Nature (London) **400**, 184 (1999).

[53] See Supplemental Material at http://link.aps.org/supplemental/10.1103/PhysRevX.14.041002 for Supplemental Videos.

[54] L. Giomi, *Geometry and topology of turbulence in active nematics*, Phys. Rev. X **5**, 031003 (2015).

[55] S. L. Anna, N. Bontoux, and H. A. Stone, *Formation of dispersions using "flow focusing" in microchannels*, Appl. Phys. Lett. **82**, 364 (2003).

[93] A. Singh, P. Incardona, and I. F. Sbalzarini, *A C++ expression system for partial differential equations enables generic simulations of biological hydrodynamics*, Eur. Phys. J. E **44**, 117 (2021).

[56] D. D. Hackney and W. Jiang, *Assays for kinesin microtubule-stimulated AT pase activity*, Methods Mol. Biol. **164**, 65 (2001).

[57] D. T. Chen, M. Heymann, S. Fraden, D. Nicastro, and Z. Dogic, *ATP consumption of eukaryotic flagella measured at a single-cell level*, Biophys. J. **109**, 2562 (2015).

[58] L. Radnai, R. F. Stremel, J. R. Sellers, G. Rumbaugh, and C. A. Miller, *A semi-high-throughput adaptation of the NADH-coupled atpase assay for screening small molecule inhibitors*, J. Vis. Exp **150**, e60017 (2019).

[59] B. Najma, W.-S. Wei, A. Baskaran, P. J. Foster, and G. Duclos, *Microscopic interactions control a structural transition in active mixtures of microtubules and molecular motors*, Proc. Natl. Acad. Sci. U.S.A. **121**, e2300174121 (2024).

[60] B. Martínez-Prat, J. Ignés-Mullol, J. Casademunt, and F. Sagués, *Selection mechanism at the onset of active turbulence*, Nat. Phys. **15**, 362 (2019).

[61] G. Duclos, C. Erlenkämper, J.-F. Joanny, and P. Silberzan, *Topological defects in confined populations of spindle-shaped cells*, Nat. Phys. **13**, 58 (2016).

[62] C. Blanch-Mercader, V. Yashunsky, S. Garcia, G. Duclos, L. Giomi, and P. Silberzan, *Turbulent dynamics of epithelial cell cultures*, Phys. Rev. Lett. **120**, 208101 (2018).

[63] S. Čopar, J. Aplinc, Žiga Kos, S. Žumer, and M. Ravnik, *Topology of three-dimensional active nematic turbulence confined to droplets*, Phys. Rev. X **9**, 031051 (2019).

[64] L. J. Ruske and J. M. Yeomans, *Morphology of active deformable 3D droplets*, Phys. Rev. X **11**, 021001 (2021).

[65] Kos and J. Dunkel, *Nematic bits and universal logic gates*, Sci. Adv. **8**, eabp8371 (2022).

[66] T. H. Tan, J. Liu, P. W. Miller, M. Tekant, J. Dunkel, and N. Fakhri, *Topological turbulence in the membrane of a living cell*, Nat. Phys. **16**, 657 (2020).

[67] J. Liu, J. F. Totz, P. W. Miller, A. D. Hastewell, Y.-C. Chao, J. Dunkel, and N. Fakhri, *Topological braiding and virtual particles on the cell membrane*, Proc. Natl. Acad. Sci. U.S.A. **118**, e2104191118 (2021).

[68] S. Zhou, A. Sokolov, O. D. Lavrentovich, and I. S. Aranson, *Living liquid crystals*, Proc. Natl. Acad. Sci. U.S.A. **111**, 1265 (2014).

[69] M. M. Genkin, A. Sokolov, O. D. Lavrentovich, and I. S. Aranson, *Topological defects in a living nematic ensnare swimming bacteria*, Phys. Rev. X **7**, 011029 (2017).

[70] P. C. Mushenheim, R. R. Trivedi, H. H. Tuson, D. B. Weibel, and N. L. Abbott, *Dynamic self-assembly of motile bacteria in liquid crystals*, Soft Matter **10**, 88 (2014).

[71] P. J. Foster, J. Bae, B. Lemma, J. Zheng, W. Ireland, P. Chandrakar, R. Boros, Z. Dogic, D. J. Needleman, and J. J. Vlassak, *Dissipation and energy propagation across scales in an active cytoskeletal material*, Proc. Natl. Acad. Sci. U.S.A. **120**, e2207662120 (2023).

[72] E. Arunachalam, W. Ireland, X. Yang, and D. Needleman, *Dissecting flux balances to measure energetic costs in cell biology: Techniques and challenges*, Annu. Rev. Condens. Matter Phys. **14**, 211 (2023).

[73] J. Li, J. M. Horowitz, T. R. Gingrich, and N. Fakhri, *Quantifying dissipation using fluctuating currents*, Nat. Commun. **10**, 1666 (2019).

[74] C. Battle, C. P. Broedersz, N. Fakhri, V. F. Geyer, J. Howard, C. F. Schmidt, and F. C. MacKintosh, *Broken detailed balance at mesoscopic scales in active biological systems*, Science **352**, 604 (2016).

[75] T. H. Tan, G. A. Watson, Y.-C. Chao, J. Li, T. R. Gingrich, J. M. Horowitz, and N. Fakhri, *Scale-dependent irreversibility in living matter*, arXiv:2107.05701.

[76] D. S. Seara, B. B. Machta, and M. P. Murrell, *Irreversibility in dynamical phases and transitions*, Nat. Commun. **12**, 392 (2021).

[77] C. E. Fernandez Noa, P. E. Harunari, M. J. de Oliveira, and C. E. Fiore, *Entropy production as a tool for characterizing nonequilibrium phase transitions*, Phys. Rev. E **100**, 012104 (2019).

[78] T. Tomé and M. J. de Oliveira, *Entropy production in nonequilibrium systems at stationary states*, Phys. Rev. Lett. **108**, 020601 (2012).

[79] S. B. Nicholson, L. P. García-Pintos, A. del Campo, and J. R. Green, *Time–information uncertainty relations in thermodynamics*, Nat. Phys. **16**, 1211 (2020).

[80] Y. Hara and A. Kimura, *An allometric relationship between mitotic spindle width, spindle length, and ploidy in caenorhabditis elegans embryos*, Mol. Biol. Cell **24**, 1411 (2013).

[81] C. P. Kelleher, Y. Rana, and D. J. Needleman, *Long-range repulsion between chromosomes in mammalian oocyte spindles*, arXiv:2211.00883v3.

[82] E. M. Rieckhoff, F. Berndt, M. Elsner, S. Golfier, F. Decker, K. Ishihara, and J. Brugués, *Spindle scaling is governed by cell boundary regulation of microtubule nucleation*, Curr. Biol. **30**, 4973.

[83] M. Castoldi and A. V. Popov, *Purification of brain tubulin through two cycles of polymerization–depolymerization in a high-molarity buffer*, Protein expression and purification **32**, 83 (2003).

[84] A. Hyman, D. Drechsel, D. Kellogg, S. Salser, K. Sawin, P. Steffen, L. Wordeman, and T. Mitchison, *Preparation of modified tubulins*, in *Molecular Motors and the Cytoskeleton*, Methods in Enzymology Vol. 196 (Academic Press, New York, 1991), Chap. 39, pp. 478–485.

[85] D. S. Martin, R. Fathi, T. J. Mitchison, and J. Gelles, *FRET measurements of kinesin neck orientation reveal a structural basis for processivity and asymmetry*, Proc. Natl. Acad. Sci. U.S.A. **107**, 5453 (2010).

[86] E. C. Young, H. K. Mahtani, and J. Gelles, *One-headed kinesin derivatives move by a nonprocessive, low-duty ratio mechanism unlike that of two-headed kinesin*, Biochemistry **37**, 3467 (1998).

[87] E. Grelet and S. Fraden, *What is the origin of chirality in the cholesteric phase of virus suspensions?*, Phys. Rev. Lett. **90**, 198302 (2003).

[88] A. M. Tayar, L. M. Lemma, and Z. Dogic, *Assembling microtubule-based active matter active matter*, in *Microtubules: Methods and Protocols* (Springer, New York, 2022), pp. 1511–83, 10.1007/978-1-0716-1983-4_10.

[89] B. Renault, R. Ragot, N. Lesevre, and A. Remond, *Onset and offset of brain events as indices of mental chronometry*, Science **215**, 1413 (1982).

[90] A. D. Edelstein, M. A. Tsuchida, N. Amodaj, H. Pinkard, R. D. Vale, and N. Stuurman, *Advanced methods of microscope control using μ manager software*, J. Biol. Methods **1**, e10 (2014), https://polscientific.com/journal/JBM/1/2/10.14440/jbm.2014.36.

[91] W. Thielicke and R. Sonntag, *Particle image velocimetry for matlab: Accuracy and enhanced algorithms in PIVlab*, J. Open Res. Software **9**, 12 (2021).

[92] A. Singh, P. H. Suhrcke, P. Incardona, and I. F. Sbalzarini, *A numerical solver for active hydrodynamics in three dimensions and its application to active turbulence*, Phys. Fluids **35**, 105155 (2023).

[94] P. Incardona, A. Leo, and Y. Zaluzhnyi, *OpenFPM: A scalable open framework for particle and particle-mesh codes on parallel computers*, Comput. Phys. Commun. **241**, 155 (2019).

[95] B. Schrader, S. Reboux, and I. F. Sbalzarini, *Discretization correction of general integral PSE operators for particle methods*, J. Comput. Phys. **229**, 4159 (2010).

[96] S. Balay, W. D. Gropp, L. C. McInnes, and B. F. Smith, *Efficient management of parallelism in object-oriented numerical software libraries*, in *Modern Software Tools for Scientific Computing*, edited by E. Arge, A. M. Bruaset, and H. P. Langtangen (Birkhäuser, Boston, 1997), pp. 163–202.